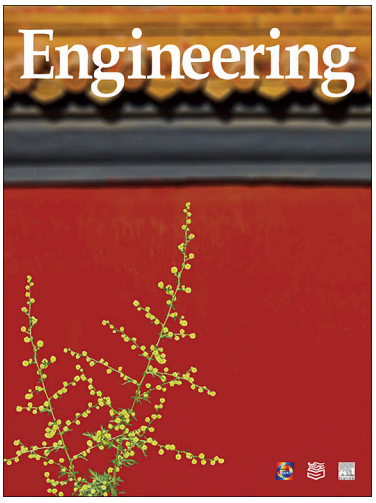
Journal Pre-proofs



Article

Multi-Criteria Evaluation of Lunar Regolith Minerals for *In-Situ* Thermal Manufacturing and Feedstock Beneficiation

Zekai Wang, Fen Dang, Wucheng Sun, Yan Zhou, Cheng Zhou, Chunze Yan, Yusheng Shi, Lieyun Ding

PII: S2095-8099(26)00559-X
DOI: https://doi.org/10.1016/j.eng.2026.09.011
Reference: ENG 2473

To appear in: *Engineering*

Received Date: 23 April 2026
Revised Date: 5 July 2026
Accepted Date: 21 September 2026

Please cite this article as: Z. Wang, F. Dang, W. Sun, Y. Zhou, C. Zhou, C. Yan, Y. Shi, L. Ding, Multi-Criteria Evaluation of Lunar Regolith Minerals for *In-Situ* Thermal Manufacturing and Feedstock Beneficiation, *Engineering* (2026), doi: https://doi.org/10.1016/j.eng.2026.09.011

This is a PDF of an article that has undergone enhancements after acceptance, such as the addition of a cover page and metadata, and formatting for readability. This version will undergo additional copyediting, typesetting and review before it is published in its final form. As such, this version is no longer the Accepted Manuscript, but it is not yet the definitive Version of Record; we are providing this early version to give early visibility of the article. Please note that Elsevier's sharing policy for the Published Journal Article applies to this version, see: https://www.elsevier.com/about/policies-and-standards/sharing#4-published-journal-article. Please also note that, during the production process, errors may be discovered which could affect the content, and all legal disclaimers that apply to the journal pertain.

© 2026 THE AUTHORS. Published by Elsevier LTD on behalf of Chinese Academy of Engineering and Higher Education Press Limited Company

Journal Pre-proofs

Res

Civil Engineering—Article

Multi-Criteria Evaluation of Lunar Regolith Minerals for *In-Situ* Thermal Manufacturing and Feedstock Beneficiation

Zekai Wang [a,#], Fen Dang [a,#], Wucheng Sun [a], Yan Zhou [a,b,*], Cheng Zhou [a], Chunze Yan [b], Yusheng Shi [b], Lieyun Ding [a]

[a] *National Center of Technology Innovation for Digital Construction, School of Civil and Hydraulic Engineering, Huazhong University of Science and Technology, Wuhan 430074, China*

[b] *State Key Laboratory of Material Processing and Die & Mold Technology, School of Materials Science and Engineering, Huazhong University of Science and Technology, Wuhan 430074, China*

*Corresponding author.
Email address: yanzhou@hust.edu.cn (Zhou Y)
[#] These authors contributed equally to this work.

Abstract

The heterogeneous mineral composition of lunar regolith significantly influences its thermal forming behavior, posing challenges for *in-situ* resource utilization (ISRU) in lunar construction. This study characterizes fifteen mineral phases identified from Chang'e-5 and Chang'e -6 returned samples and evaluates the manufacturing suitability of the ten complete-data minerals for three representative thermoforming processes: hot-press sintering (HPS), microwave sintering (MWS), and selective laser melting (SLM). Eight thermophysical properties (solidus temperature, specific heat capacity, thermal conductivity, melt viscosity, surface tension, density, dielectric loss tangent, and solar absorptivity) were characterized for all fifteen minerals. A multi-criteria decision-making framework integrating fuzzy-analytic hierarchy process (AHP)–entropy multiplicative weighting was developed to determine process-specific parameter weights, and the mineral suitability was ranked using dual TOPSIS–VIKOR methods. The combined weights identified thermal conductivity (33.7%) as the dominant parameter for HPS, dielectric loss tangent (57.3%) for MWS, and solar absorptivity (33.0%) for SLM, reflecting the distinct heat transfer mechanisms of each process. For the ten complete-data minerals, a process-specific suitability ranking was established, identifying ilmenite as the only universally superior ranked mineral, the pyroxene group as favorable for HPS and SLM, and the feldspar group as consistently unfavorable across the three processes. Sensitivity analyses (Monte Carlo weight perturbation and VIKOR v-parameter variation) confirmed the robustness of the rankings. Gradient blending experiments validated the predictions at both macroscopic and microscopic scales, with cross-process density correlation yielding Pearson r = 0.788 (p = 0.002) and Spearman ρ = 0.825 (p = 0.001), and within-process rank agreement of ρ = 1.000 for all three processes. The findings provide first-order guidance for mineral beneficiation strategies, manufacturing process selection, and preliminary landing-site evaluation in future lunar base construction.

Keywords

Lunar regolith minerals; Thermophysical properties; Multi-criteria decision-making (MCDM); Fuzzy-AHP; TOPSIS

1. Introduction

Lunar base construction is essential for sustaining long-term deep space exploration activities. A permanent lunar habitat must provide structural support as well as comprehensive protection against the vacuum environment, meteoroid impacts, and cosmic radiation [1,2]. Given the prohibitive cost of Earth-to-Moon material transportation, *in-situ* resource utilization (ISRU), and particularly the fabrication of structural components directly from lunar regolith, has emerged as the most viable and sustainable construction strategy. Among the available ISRU fabrication approaches, sintering and melting processes offer the advantages of high material utilization efficiency and mechanical strength, making them promising candidates for infrastructure elements such as launch/landing pads [3,4] and hardened pavements [5].

Three representative thermal manufacturing processes have been extensively investigated for lunar regolith forming: hot-press sintering (HPS), microwave sintering (MWS), and selective laser melting (SLM). Although all three processes consolidate loose regolith particles into dense solids through thermal energy input [6], their underlying heat transfer mechanisms differ fundamentally. In HPS [7–9], heat is generated by external resistive elements and conducted inward from the die walls through the powder compact—a surface-to-core process governed by thermal conductivity. In MWS [10–13], the material self-heats volumetrically through dielectric energy dissipation: The alternating electromagnetic field at 2.45 GHz induces dipole polarization and molecular rotation within the regolith, converting microwave energy directly into thermal energy throughout the bulk. In SLM [14–17], a focused laser beam delivers highly localized energy to the powder bed surface; the absorbed photon energy is instantaneously converted to heat, generating a small melt pool in which heat transfer is dominated by conduction and convection. These distinct mechanisms imply that the thermophysical properties governing densification success differ from process to process.

Journal Pre-proofs

The quality of sintered or melted lunar regolith components, including strength, uniformity, and porosity, is strongly depe[illegible]cally available mineral resources [20]. Orbital remote sensing has enabled the mapping of chemical and mineralogical distributions across the lunar surface, providing critical data for identifying regions enriched in specific minerals favorable for ISRU manufacturing [21]. Furthermore, given the inherent heterogeneity of lunar regolith, a direct "excavate-and-use" approach is unlikely to yield consistent manufacturing outcomes. Instead, mineral beneficiation should be employed to selectively enrich favorable mineral components and tailor the feedstock composition to the requirements of each forming process [22–24], thereby enabling performance-controlled fabrication of lunar regolith components. Beneficiation provides a practical route for regulating the mineralogical composition of lunar regolith feedstocks before thermal manufacturing. Previous studies have summarized physical beneficiation methods such as particle-size classification, magnetic separation, electrostatic separation, and density/gravity-based separation [25], and recent work has shown their potential for ilmenite enrichment and improved processing of lunar regolith simulants [26–28]. In this study, beneficiation is therefore considered as a composition-control step that links mineral suitability ranking with process-specific feedstock preparation. However, the lunar regolith comprises a complex assemblage of silicates, oxides, and impact/volcanic glasses, each exhibiting distinct thermophysical characteristics [29,30]. Current research on the influence of regolith composition on thermal forming has focused predominantly on individual minerals or simplified binary systems, and a systematic, multi-mineral evaluation framework applicable across multiple manufacturing processes remains lacking.

In this study, fifteen mineral phases representative of the lunar regolith, identified from Chang'e-5 and Chang'e-6 return samples, were systematically characterized for eight thermophysical properties relevant to ISRU manufacturing. A multi-criteria decision-making (MCDM) framework integrating fuzzy-analytic hierarchy process (AHP) with entropy weighting through multiplicative normalization was developed to evaluate the suitability of these minerals for three representative thermal manufacturing processes: HPS, MWS, and SLM. The ranking results, cross-validated by order preference by similarity to ideal solution (TOPSIS) and VIseKriterijumska Optimizacija I Kompromisno Resenje (VIKOR) methods, were further confirmed through gradient blending experiments using both macroscopic densification and microscopic sintering neck measurements. The findings provide first-order process-design guidance for mineral-specific feedstock selection and preliminary landing-site evaluation in future lunar base construction.

2. Materials and methods

2.1 Mineral summary of samples returned from the moon

Lunar soil is the main raw material for the production of lunar building materials. Using remote sensing and experiments on real samples, the mineral composition of the moon has been studied. The mineral composition of the moon is much less than that of the earth. is the moon lacks water and chemical weathering, resulting in no water-bearing minerals or clay minerals. In recent years, China's Chang'e-5 and Chang'e-6 have carried 1731 g of the lunar mare sample and 1935.3 g of the lunar farside sample back to the earth. At present, studies have reported about dozens of different lunar soil minerals, among which the content of feldspar and pyroxene is higher, accounting for more than 30%, and a certain amount of olivine and ilmenite. In addition to common minerals, there are also a small amount of quartz, potassium feldspar, apatite, and other substances in the lunar soil. In the study of lunar regolith samples, Changesite-(Y), cristobalite, stishovite, and few-layer graphene were also discovered for the first time. It is worth noting that there are also a large number of amorphous glasses in the lunar regolith, including impact glass and volcanic glass. The minerals and contents reported in Chang'e-5 and Chang'e-6 samples are shown in Table 1 [31–41].

Table 1.
Common minerals in lunar soil.

Category	Mineral	Chemical formula	Content (wt% CE-5) [31]	Content (wt% CE-6) [32]
Olivine group	Forsterite [33]	Mg_2SiO_4	1.6	0.6
	Fayalite [33]	Fe_2SiO_4	4.1	
Pyroxene group	Augite [34]	$Ca(Mg, Fe, Al)(Si, Al)_2O_6$	30.9	19.7
	Clinopyroxene [31]	$(Ca, Mg, Fe)(Mg, Fe)Si_2O_6$	11.1	10.2
	Orthopyroxene [35]	$(Mg, Fe)_2Si_2O_6$	n.r.	3.7
Plagioclase group	Anorthite [34]	$CaAl_2Si_2O_8$	30.1	32.9
	Albite [34]	$NaAlSi_3O_8$		
Oxide	Ilmenite [34]	$FeTiO_3$	4.5	1.8
	Spinel [34]	$MgAl_2O_4$	n.r.	n.r.
	Chromite [36]	$FeCr_2O_4$	n.r.	n.r.
	Baddeleyite [34]	ZrO_2	n.r.	n.r.

Journal Pre-proofs

	Quartz [34]	SiO_2	0.4	n.r.
	K-feldspar [34,35]	$KAlSi_3O_8$	n.r.	n.r.
	Apatite [34]	$Ca_5(PO_4)_3(F, Cl)$	0.7	n.r.
Phosphate	Merrillite [37]	$Ca_9NaMg(PO_4)_7$	n.r.	n.r.
	Changesite-Y [38]	$(Ca_8Y)\square Fe^{2+}(PO_4)_7$ (where □ denotes a vacancy)	n.r.	n.r.
	Zircon [39]	$ZrSiO_4$	n.r.	n.r.
	Troilite [34]	FeS	n.r.	n.r.
Sulfide	Ferronickel [40]	FeNi	n.r.	n.r.
	Zirconolite [37]	$CaZrTi_2O_7$	n.r.	n.r.
	Cristobalite [41]	SiO_2	n.r.	n.r.
	Seifertite [41]	SiO_2	n.r.	n.r.
	Stishovite [41]	SiO_2	n.r.	n.r.
	Glass [31]	—	16.6	27.9

n.r.: not reported; the phase is documented in the Chang'e-5/Chang'e-6 samples (CE-5/CE-6) but no quantitative content is given in the cited sources. Values are listed as reported in those sources.

2.2 Methodology

This study adopts a systematic, multi-step methodological framework to evaluate the suitability of lunar regolith minerals for *in-situ* manufacturing via three representative thermal forming techniques (Fig. 1). Step 1 (mineral collection) compiles fifteen lunar regolith simulant minerals covering the primary mineralogical components identified from Chang'e-5 and Chang'e-6 returned samples. Step 2 (thermophysical properties testing) characterizes eight key parameters critical to manufacturing performance—solidus temperature (T_s), specific heat capacity (C_p), thermal conductivity (κ), melt viscosity (η), surface tension (γ), density (ρ), dielectric loss tangent (tan δ), and solar radiation absorptivity (α_{solar})—providing a quantitative foundation for subsequent analysis. Step 3 (weight calculation by Fuzzy-AHP and entropy weight method) establishes process-specific parameter weights through a combination of subjective expert judgment (Fuzzy-AHP with three-expert geometric mean fusion) and objective data-driven analysis (entropy weighting), merged via multiplicative normalization to enforce a dual-screening mechanism. Step 4 (mineral classification by TOPSIS and VIKOR) integrates the combined weights with the thermophysical data to rank minerals using dual MCDM methods—TOPSIS and VIKOR—with ranking robustness verified by Monte Carlo weight perturbation and VIKOR v-parameter sensitivity analysis. Step 5 (experimental validation of representative minerals) confirms the ranking predictions through gradient blending experiments, in which the top-ranked and bottom-ranked minerals are blended with the CUG-1A (a type of lunar regolith simulant produced by China University of Geosciences (Wuhan)) baseline simulant at ±10% and ±20% levels, and the manufacturing outcomes are evaluated by relative density, porosity, sintering degree, surface roughness, and hardness across the three processes.

Journal Pre-proofs

Journal Pre-proofs

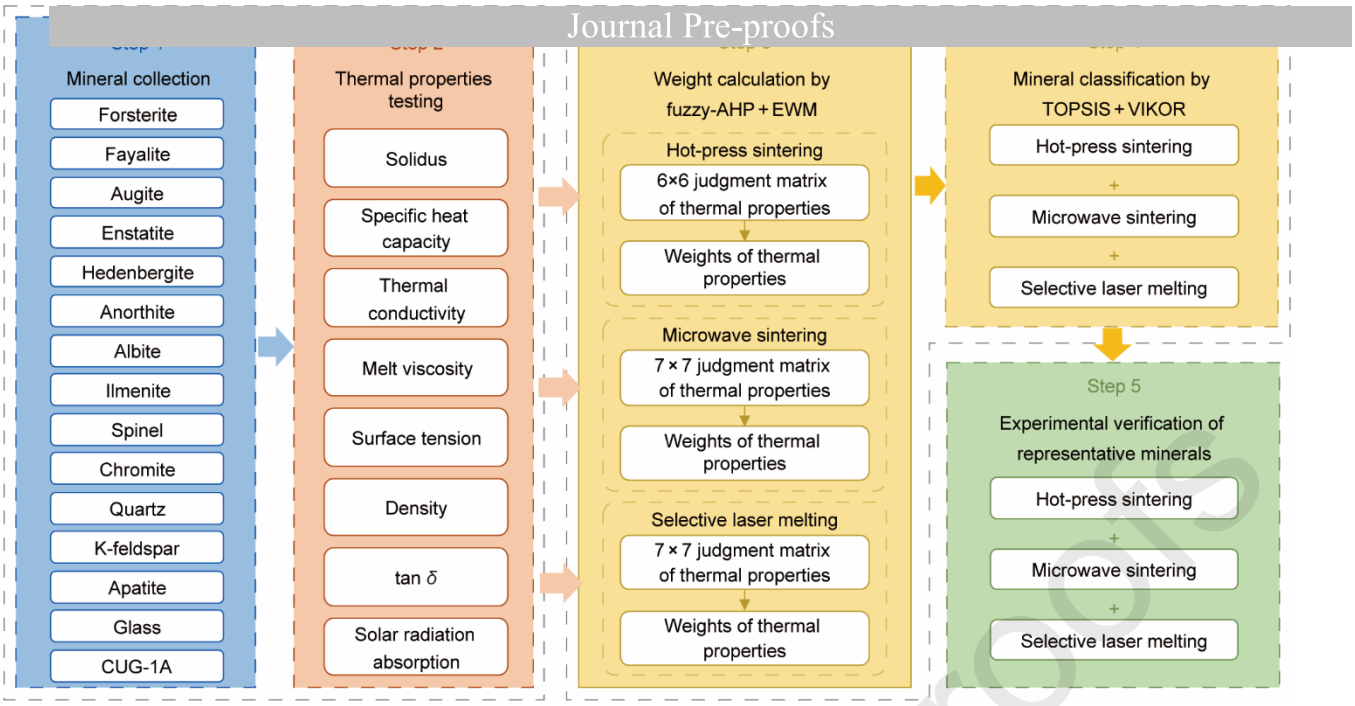


Fig.1 Schematic diagram of a multi-step methodology framework. EWM: entropy weight method.

2.2.1 Material collection

The fifteen phases evaluated here were selected from the minerals reported in the Chang'e-5 and Chang'e-6 samples in Table 1 on the basis of modal abundance, coverage of the principal rock-forming groups that govern thermal forming, namely plagioclase, pyroxene, olivine, ilmenite, and glass, and the widest possible span of the eight thermophysical properties from Fe/Ti-bearing oxides to framework aluminosilicates. Feldspar and pyroxene each exceed 30 wt% and, with olivine, ilmenite, and glass, dominate the regolith, whereas unselected phases such as merrillite, troilite, Fe–Ni metal, Zr-bearing phases, the rare silica polymorphs and Changesite-(Y) occur only at trace levels, contribute negligibly to the bulk thermophysical response, and often have no commercially available phase-pure analogue. The selected minerals were purchased through commercial channels and their morphology is shown in Fig. 2, comprising forsterite, fayalite, augite, enstatite, hedenbergite, ilmenite, anorthite, albite, K-feldspar, quartz, apatite, spinel, and chromite. Their authenticity was verified by laser confocal Raman spectroscopy (LabRAM HR800, HORIBA Jobin Yvon, Japan) against the corresponding reference spectra in the RRUFF database, as shown in Fig. 3.

Journal Pre-proofs

Journal Pre-proofs



Fig. 2 Morphology of different minerals.

The use of terrestrial minerals is justified because the eight evaluated properties are governed by crystal structure, bonding, and major-element chemistry, which are intrinsic to a mineral species and shared between its terrestrial and lunar occurrences rather than set by provenance. A structurally and compositionally faithful specimen, confirmed here as the correct phase by Raman verification against the RRUFF database, therefore reproduces the same governing thermophysical behavior as its lunar counterpart. Lunar minerals differ only in second-order respects such as higher Fe content, anhydrous character, and space-weathering features, which mainly rescale absolute values and have limited effect on the relative ranking.

The standard lunar regolith simulant selected for the experiments was the CUG-1A lunar regolith simulant developed by the China University of Geosciences (Wuhan, China), and its chemical and mineral compositions are shown in Table S1 in Appendix A. The minerals were subjected to a thorough washing process, followed by a drying procedure. Thereafter, they were meticulously hand-selected and subsequently ground into a powder using a ball mill. In order to eliminate the potential impact of particle size on the physical properties of the mineral powder and the lunar regolith simulant, both samples were subjected to a sieving process using a 200-mesh sieve.

Journal Pre-proofs

Journal Pre-proofs

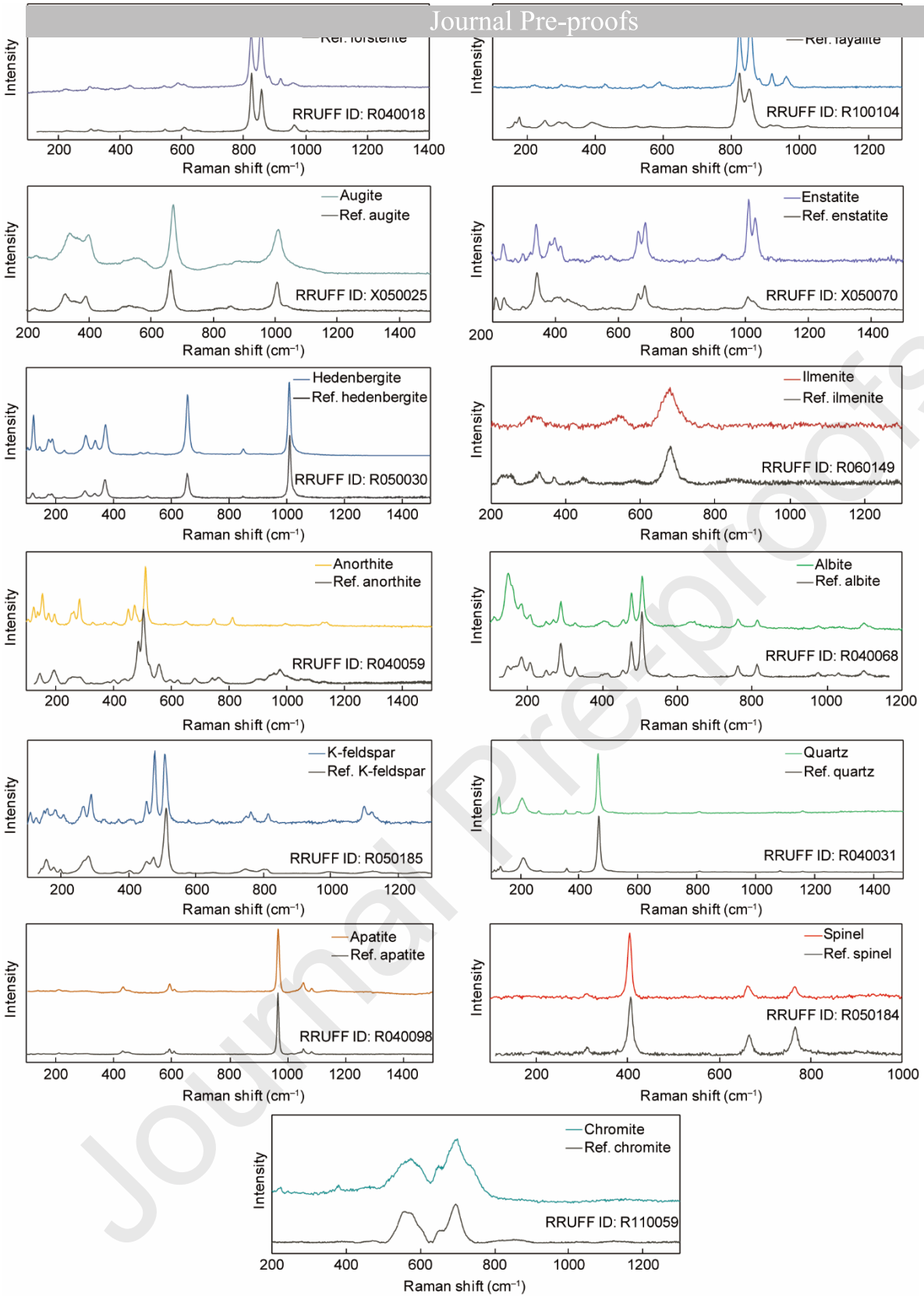


Fig.3 Raman spectra and standard comparison of common minerals in lunar regolith.

2.2.2 Thermal properties testing

The solidus temperatures of the minerals and lunar regolith simulant were determined by hot-stage microscopy (HSM) using a Dataphysics OCA25-HTV1800 instrument (Germany). Cylindrical specimens were heated from room temperature to 1650 °C at a rate not exceeding 6 °C · min^{-1} under ambient atmosphere. The silhouette profiles were recorded at regular temperature intervals, and T_s was identified as the onset temperature of the first observable deformation. The surface tension coefficients were subsequently calculated from the sessile drop profile of the fully molten specimen using the Young–Laplace equation. The solidus temperature of lunar regolith simulant was obtained using a combined thermogravimetric/differential

thermal analyser (STA449F3) (NETZSCH-Gerätebau GmbH, Germany)with a temperature increase rate of 20 °C·min^{-1} and an a

Journal Pre-proofs

The specific heat capacity and thermal diffusion coefficient of the minerals and lunar regolith simulant were measured using a Diamond differential scanning calorimeter (DSC) differential scanning calorimeter (PerkinElmer Instruments, USA; American Society for Testing and Materials (ASTM) E1269) and an LFA 467 HT HyperFlash® laser flash apparatus (NETZSCH Instruments, Germany; ASTM E1461), respectively. The thermal conductivity was then calculated using Eq. (S1) in Appenddix A. Both C_p and κ were characterized over the range 25–200 °C. Because the TOPSIS/VIKOR procedure requires a single, internally consistent decision matrix, one reference temperature was adopted for the multi-criteria analysis. The value at 75 °C was selected, as it lies within the measured range and corresponds to a state in which all minerals are fully solid and crystalline, providing an internally consistent basis for cross-mineral comparison; near each mineral's solidus (T_s = 1091–1645 °C), mineral-specific softening, devitrification, and incipient melting would distort C_p and κ in a non-comparable manner. The robustness of this choice is examined in Section 3.1. The densities of the thirteen natural mineral phases were adopted from established mineralogical reference data [42]. For minerals exhibiting compositional variability (e.g., augite, enstatite, chromite), the midpoint of the reported density range was used. The viscosity of mineral and lunar regolith simulant samples was measured using a high temperature viscometer BCT1700 (Shanghai Huanao, China), with a ramp rate of 20°C·min^{-1} and an argon atmosphere. The real and imaginary parts of the complex permittivity of minerals and lunar regolith simulants over 2–18 GHz were measured at room temperature by a vector network analyzer (VNA, Keysight N5244B PNA-X (Keysight Technologies, USA)) in coaxial mode, and the dielectric loss tangent (tan δ) used in the MCDM analysis was extracted at the microwave-sintering frequency of 2.45 GHz. The use of a room-temperature value, and its validity for ranking purposes, is discussed in Section 4.2.

The spectral absorptance of each mineral was measured over the wavelength range of 280–2500 nm using a SolidSpec-3700 ultraviolet (UV)–visible(Shimadzu Corporation, Japan) near-infrared spectrophotometer (wavelength accuracy: ±0.1 nm; photometric accuracy: ±0.003 absorbance (Abs)). The total solar radiation absorptivity (α_{solar}) was then calculated by integrating the product of the measured spectral absorptance and the air mass zero (AM0) solar irradiance spectrum over the full wavelength range [43].

2.2.3 Weight calculation by Fuzzy-AHP and EWM

The relative importance of thermophysical parameters varies across manufacturing processes. For instance, dielectric loss tangent dominates microwave energy coupling but is irrelevant to HPS. Therefore, process-specific weight vectors were established through a combination of subjective expert judgment and objective data-driven analysis, then merged via multiplicative normalization.

(1) Subjective weighting: Fuzzy-AHP. Three experts independently constructed pairwise comparison matrices for each process using the Saaty 1-9 scale, converted to triangular fuzzy numbers (l, m, u) [44–46] as shown in Table S2. The matrix dimensions are 6 × 6 for HPS (T_s, C_p, κ, η, γ, ρ) and 7 × 7 for MWS (adding tan δ) and SLM (adding α_{solar}). The three individual fuzzy matrices were fused via geometric mean:

$$\tilde{a}_{ij}^{\text{group}} = \left(\tilde{a}_{ij}^{(1)} \otimes \tilde{a}_{ij}^{(2)} \otimes \tilde{a}_{ij}^{(3)}\right)^{\frac{1}{3}} (1)$$

where i and j denote the row and column indices, respectively, corresponding to the i and j criteria in the pairwise comparison matrix (i, j=1,2,…, n), and n is the total number of criteria. The fused matrix was de-fuzzified by extracting the m-values, and priority weights were derived via the eigenvalue method. Finally, a consistency test is performed using Eq. (S2) in Appendix A. If the consistency ratio CR < 0.1, the matrix passes the consistency test.

(2) Objective weighting: Entropy Weight Method. The entropy weight method (EWM) [47,48] derives parameter weights from the statistical dispersion of the measured data, independent of expert judgment. Parameters with greater variation across the candidate set carry higher information content (lower entropy) and are assigned higher weights. This approach complements Fuzzy-AHP by capturing data-driven distinctions that expert judgment may overlook. Because five high-melting minerals did not reach a stable molten state within the effective upper temperature limit of the high-temperature testing system, their solidus temperature, melt viscosity, and surface tension could not be reliably determined. The entropy-weight calculation was therefore performed using the ten complete-data alternatives across all decision parameters.

It should be emphasized that the entropy weights are dataset-dependent. In the present study, they quantify the relative discriminating power of each parameter within the decision matrix formed by the ten complete-data alternatives, rather than representing universal process-importance weights for all lunar-regolith mineral systems. This is consistent with the standard use of the entropy-weight method, in which parameters with larger information contrast among the candidate alternatives

Journal Pre-proofs

Journal Pre-proofs

receive higher objective weights. Therefore, the entropy weights are interpreted here as sample-specific information weig… …s the standard entropy weighting algorithm: ① min–max normalization of the decision matrix; ② computation of probability matrices; ③ calculation of information entropy for each parameter; and ④ derivation of weights from the diversity coefficients (1 − entropy).

(3) **Combined weighting: Multiplicative normalization.** The subjective (Fuzzy-AHP (FAHP)) and objective (EWM) weight vectors (***W***) were combined using multiplicative normalization [49]:

$$\boldsymbol{W}_k^{\text{combined}} = \frac{\boldsymbol{W}_k^{\text{FAHP}} \times \boldsymbol{W}_k^{\text{EWM}}}{\sum_{k=1}^{n} \boldsymbol{W}_k^{\text{FAHP}} \times \boldsymbol{W}_k^{\text{EWM}}}$$

where *k* denotes the position of a certain thermal property parameter in the weight vector, and *n* is the total number of thermal property parameters in the vector. This approach enforces a "dual-screening" mechanism: A parameter receives a high combined weight only when both expert judgment and data dispersion agree on its importance. If either source assigns a low weight, the product is suppressed. This dual-screening interpretation also prevents the combined weight from being controlled by data dispersion alone. A parameter with high variance but weak process relevance is suppressed by the Fuzzy-AHP term, whereas a parameter judged important by experts but showing little contrast among the candidate alternatives is suppressed by the entropy term. Thus, the combined weight is interpreted as a process-specific discriminating weight that jointly reflects physical relevance and dataset-level information contrast, rather than as a purely variance-driven coefficient. This is physically intuitive—a parameter that is theoretically important but shows little variation among the minerals under study (e.g., T_s) will have its combined weight moderated, while a parameter that is both physically critical and highly discriminating (e.g., tan δ for MWS) would be amplified. Multiplicative normalization was preferred over game-theory combination weighting for two reasons. In the two-source case the optimal combination coefficients obtained from game-theory weighting typically yield weights close to a simple average, so the additional optimization brings little practical gain. Multiplicative normalization also enforces a clearer dual-screening logic, in which a parameter is amplified only when both the subjective and objective sources rank it highly and is suppressed if either source assigns it a low weight, which is more directly interpretable for the present application.

2.2.4 Mineral classification by TOPSIS and VIKOR

2.2.4.1 TOPSIS ranking. The Technique for TOPSIS was applied to rank the ten minerals with complete data for each process [50]. The decision matrix was first normalized by the vector method, then multiplied by the combined weights from Section 2.2.3. The positive ideal solution (PIS) and negative ideal solution (NIS) were identified based on the benefit or cost direction of each parameter. The closeness coefficient was computed as:

$$C_m = \frac{D_m^-}{D_m^+ + D_m^-}$$

where *m* denotes the index of the mineral being evaluated and D_m^+ and D_m^- were the Euclidean distances to the PIS and NIS, respectively. Higher C_m indicates better process suitability. The benefit/cost directions were assigned based on manufacturing physics and are summarized in Appendix A Table S4.

2.2.4.2 VIKOR cross-validation. To verify that the ranking results are independent of the specific MCDM algorithm, the VIKOR [51,52] method was applied as a cross-validation tool. VIKOR differs from TOPSIS in its mathematical foundation: While TOPSIS ranks alternatives by geometric distance to ideal solutions, VIKOR seeks a compromise solution that minimizes the group utility (weighted sum of normalized gaps) and individual regret (worst-performing parameter). The VIKOR compromise ranking index Q_m is computed as:

$$Q_m = v \cdot \frac{S_m - S^*}{S^- - S^*} + (1 - v) \cdot \frac{R_m - R^*}{R^- - R^*}$$

where S_m is the group utility, R_m is the individual regret, and *v* is the decision strategy parameter (v = 0.5 by default, representing equal emphasis on overall performance and absence of critical weaknesses). $S^- = maxS_i$ and $S^* = minS_i$ are the maximum and minimum group utility values, respectively, and $R^- = maxR_i$ and $R^* = minR_i$ are the maximum and minimum individual regret values, respectively, across all evaluated minerals. The consistency between TOPSIS and VIKOR rankings was assessed using the Spearman rank correlation coefficient ρ, with $\rho > 0.85$ and $p < 0.05$ indicating high agreement.

2.2.4.3 Sensitivity analysis. Two types of sensitivity analyses were conducted to verify the robustness of the ranking results:

(1) **Monte Carlo weight perturbation**: The combined weight vector was subjected to ±20% random perturbation following a normal distribution (mean = 1.0, standard deviation = 0.20), and 10 000 TOPSIS iterations were performed for

each process. The ranking stability was assessed by the standard deviation of each mineral's rank across all iterations, with σ < 1.

Journal Pre-proofs

(2) **VIKOR *v*-parameter sensitivity**: The VIKOR decision strategy parameter v was varied from 0.3 to 0.7 (in increments of 0.1) to examine whether the ranking changes when the decision maker shifts emphasis between "overall best performance" (high v) and "minimizing the worst weakness" (low v). A ranking fluctuation range ≤ 1 was considered stable.

2.2.5 Experimental validation of representative minerals

To experimentally verify the TOPSIS predictions, gradient blending tests were designed for each manufacturing process. The equipment used for the three forming methods was self-developed by Huazhong University of Science and Technology. For HPS and MWS, the powders were placed in graphite moulds with a mould size of Φ10 mm × 20 mm and cold pressed to increase their packing density before sintering. The HPS parameters were as follows: holding at 1150 °C for 1 h, followed by natural cooling, under a vacuum of 40 Pa. The MWS parameters were as follows: holding at 1150 °C for 0.5 h, followed by natural cooling, at a microwave frequency of 2.45 GHz. SLM was performed on a self-developed large-spot system at a coarser scale than commercial powder-bed SLM. The laser power was 200 W and the scanning speed was 5 mm·s^{-1}. The laser spot diameter was 2 mm, and the hatch spacing between adjacent tracks was set equal to it at 2 mm to give full coverage of each layer. The part was built layer by layer with a powder layer thickness of 2 mm per layer, using a vertical scanning strategy. These larger length scales are dictated by the coarse regolith feedstock and the self-developed equipment.

One independent specimen was fabricated for each composition and process, yielding five specimens per process and fifteen specimens in total. For each specimen, the reported density and porosity were averaged over three backscattered-electron image fields, the sintering degree over three particle pairs, and the surface roughness over nine measurement areas, so that each value reflects within-specimen variability rather than a single measurement. Vickers hardness was further measured as an additional mechanical-performance indicator using an Innovatest Falcon 507 hardness tester following GB/T 4340.1–2024. A Vickers load of HV1, corresponding to a 1 kilogram-force (kgf, 1 kgf ≈ 9.807 N) test force, was applied with a dwell time of 15 s. For each specimen, three indentations were performed at different positions. These gradient blending experiments were designed as controlled single-mineral perturbations of the multicomponent CUG-1A matrix, rather than as a complete representation of nonlinear phase interactions in real multiphase lunar regolith.

3. Results

3.1 Analysis of thermophysical properties of minerals

The measured thermophysical properties of all fifteen minerals are presented as a standardized heatmap in Fig. 4, where each cell represents the Z-score normalized value of a given parameter for a given mineral. This visualization reveals several prominent patterns in the dataset.

Solidus temperatures ranged from 1091 °C (glass) to 1645 °C (fayalite), spanning over 550 °C across the mineral set. As shown in Fig. 5, the distribution shows a clear compositional dependence: iron-rich minerals with simple crystal structures (fayalite, ilmenite) exhibited the highest T_s values (1550–1645°C), while the glass phase showed the lowest T_s (1091 °C) owing to its amorphous structure and lack of long-range crystallographic order. The feldspars and pyroxenes occupied an intermediate range (1264–1450°C). For minerals with gradual softening behavior where the deformation onset was difficult to resolve at 100 °C intervals, supplementary HSM images with finer temperature steps are provided in Appendix A Fig. S1. For CUG-1A, the DSC onset temperature (1218 °C, Fig. S2(a) in Appendix A) was in close agreement with the HSM-observed deformation temperature (1225 °C), confirming the consistency between the two independent techniques. The glass phase exhibited a distinct thermal evolution in the DSC curve (Fig. S2(b)): an exothermic peak at 857 °C corresponding to devitrification (crystallization of the amorphous phase), followed by an endothermic peak at 1091 °C corresponding to the melting of the devitrification products. Unlike crystalline minerals that maintain structural rigidity until the solidus is reached, the glass phase undergoes gradual softening above the glass transition temperature (T_g), devitrification, and finally melting—a three-stage process characteristic of amorphous silicates. The T_s value of 1091 °C reported for glass therefore represents the onset of the final melting event rather than a thermodynamically defined solidus.

The specific heat capacity and thermal conductivity of all fifteen minerals as functions of temperature are presented in Appendix A Fig. S3(a) and (b), respectively. Both parameters exhibited temperature-dependent behavior, with peak values generally occurring near 75 °C before declining at higher temperatures. The 75 °C values were used as the common reference point for the subsequent MCDM analysis (Section 2.2.2). To confirm that the mineral ranking is not an artifact of this choice, the minerals were re-ranked by C_p and by κ at each measured temperature (25, 75, 125, 175, and 200 °C). The relative ordering was preserved across the entire measured range: For κ, the Spearman correlation between the 75 °C ranking and every other temperature was ρ = 0.87–0.95 (all $p < 0.05$), with a Kendall coefficient of concordance of W = 0.93 (Eqs. (S3) and (S4) in Appendix A); C_p showed comparable stability (W = 0.86). Thermal conductivity at 75 °C showed the largest relative variation among all parameters, spanning from 0.209 W·(m·°C)$^{-1}$ for K-feldspar to 0.651 W·(m·°C)$^{-1}$ for fayalite—a three-fold difference. A clear mineralogical trend emerged: The oxide and olivine groups (ilmenite, fayalite, forsterite, spinel, chromite) exhibited consistently high κ values (0.58–0.65 W·(m·°C)$^{-1}$), while the feldspar and silica groups (K-feldspar, quartz, anorthite, albite) clustered at the low end (0.21–0.27 W·(m·°C)$^{-1}$). The pyroxene group occupied an intermediate range (0.29–0.47 W·(m·°C)$^{-1}$). This systematic variation reflects the differences in crystal structure and bonding character: Dense, ionic-bonded oxide structures facilitate phonon transport more efficiently than the open, covalent framework silicates.

Journal Pre-proofs

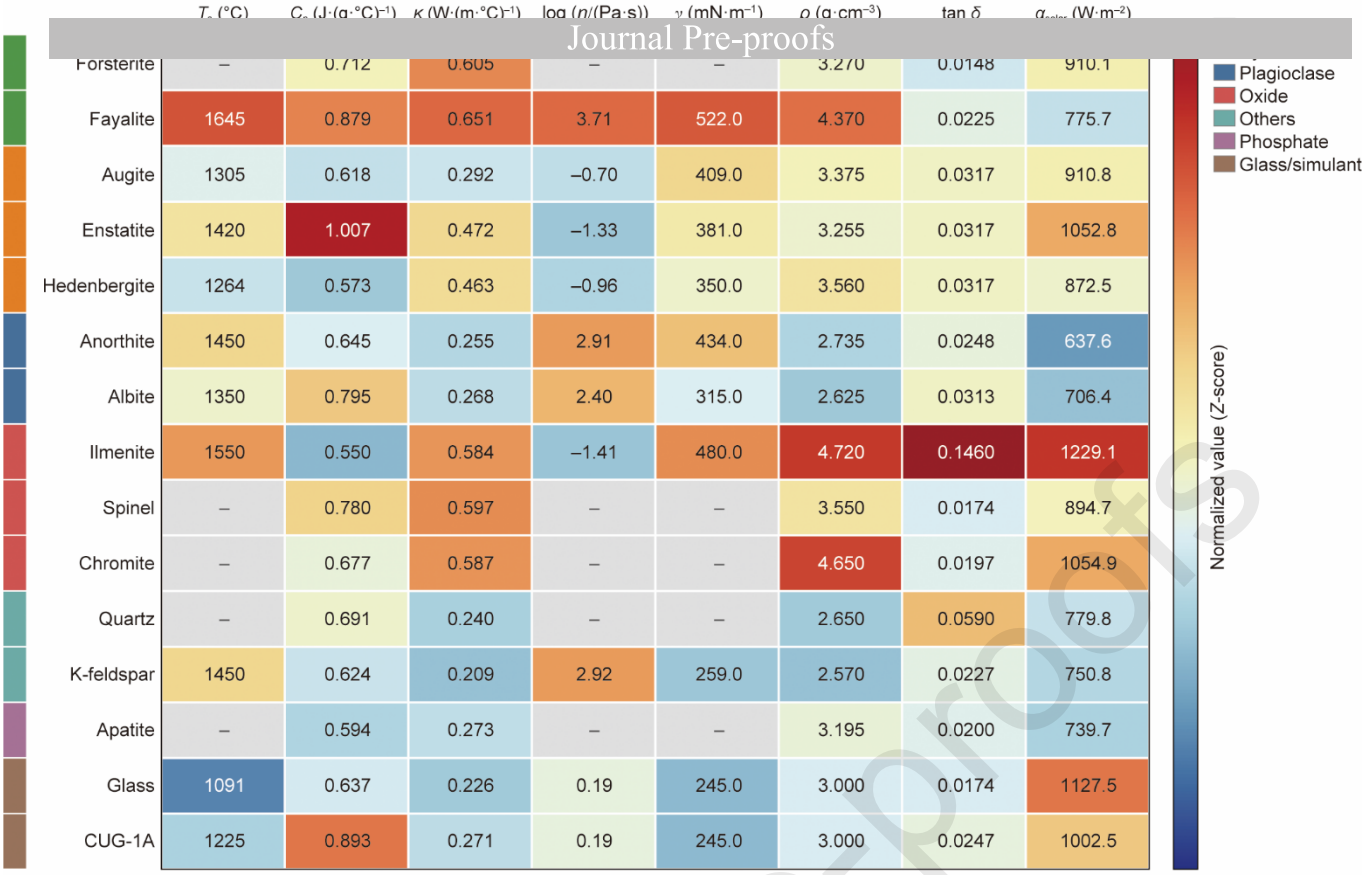


Fig.4 Thermophysical properties of fifteen lunar regolith minerals. T_s: solidus temperature; C_p: specific heat capacity; κ: thermal conductivity; η: melt viscosity (log scale); γ: surface tension; ρ: density; tan δ: dielectric loss tangent; α_{solar}: solar radiation absorptivity. Missing values indicate properties that could not be measured within the accessible temperature range.

Melt viscosity, expressed as log(η/(Pa·s)), exhibited the widest absolute range of any parameter, spanning over five orders of magnitude from −1.41 (ilmenite) to 3.71 (fayalite). As shown in Fig.S3(c) in Appendix A, minerals rich in network-forming oxides (SiO_2, Al_2O_3), particularly the feldspars (anorthite: 2.91, K-feldspar: 2.92, albite: 2.40), displayed high viscosities, consistent with the highly polymerized silicate network structure of their melts. In contrast, minerals dominated by network-modifying cations (Fe^{2+}, Mg^{2+}, Ca^{2+}), such as the pyroxenes and ilmenite, showed much lower viscosities, reflecting the depolymerized melt structure that facilitates viscous flow. The glass and CUG-1A simulant exhibited identical intermediate η values (log η = 0.19), consistent with their similar bulk compositions.

Surface tension values ranged from 245 mN·m^{-1} (glass and CUG-1A) to 522 mN·m^{-1} (fayalite). The distribution showed a gradual gradient across the mineral set rather than extreme outliers. Minerals with high iron content (fayalite, ilmenite) tended to exhibit higher surface tension, which is consistent with the strong metallic bonding contribution of Fe^{2+} at the melt–air interface. The measured values are in good agreement with previously reported surface tension data for silicate and oxide melts of comparable compositions [53–59], confirming the reliability of the sessile drop measurements employed in this study.

As shown in Fig. S4 in Appendix A, the dielectric loss tangent (tan δ) at 2.45 GHz showed a distinctive distribution dominated by a single outlier: ilmenite (0.146), which exceeded the second-highest value (quartz, 0.059) by a factor of 2.5 and the lowest value (forsterite, 0.015) by nearly ten-fold. This extreme dispersion reflects the unique contribution of Fe^{2+}-Ti^{4+} charge transfer and electronic conduction mechanisms in the ilmenite crystal structure, which are absent in silicate minerals. Because this is an intrinsic electronic loss channel rooted in the mixed-valence crystal structure, it is already active at room temperature; the long-standing observation that oxide minerals such as ilmenite couple strongly to microwaves while silicates remain largely transparent [60] confirms that this contrast is structural rather than an artifact of the measurement temperature.

Journal Pre-proofs

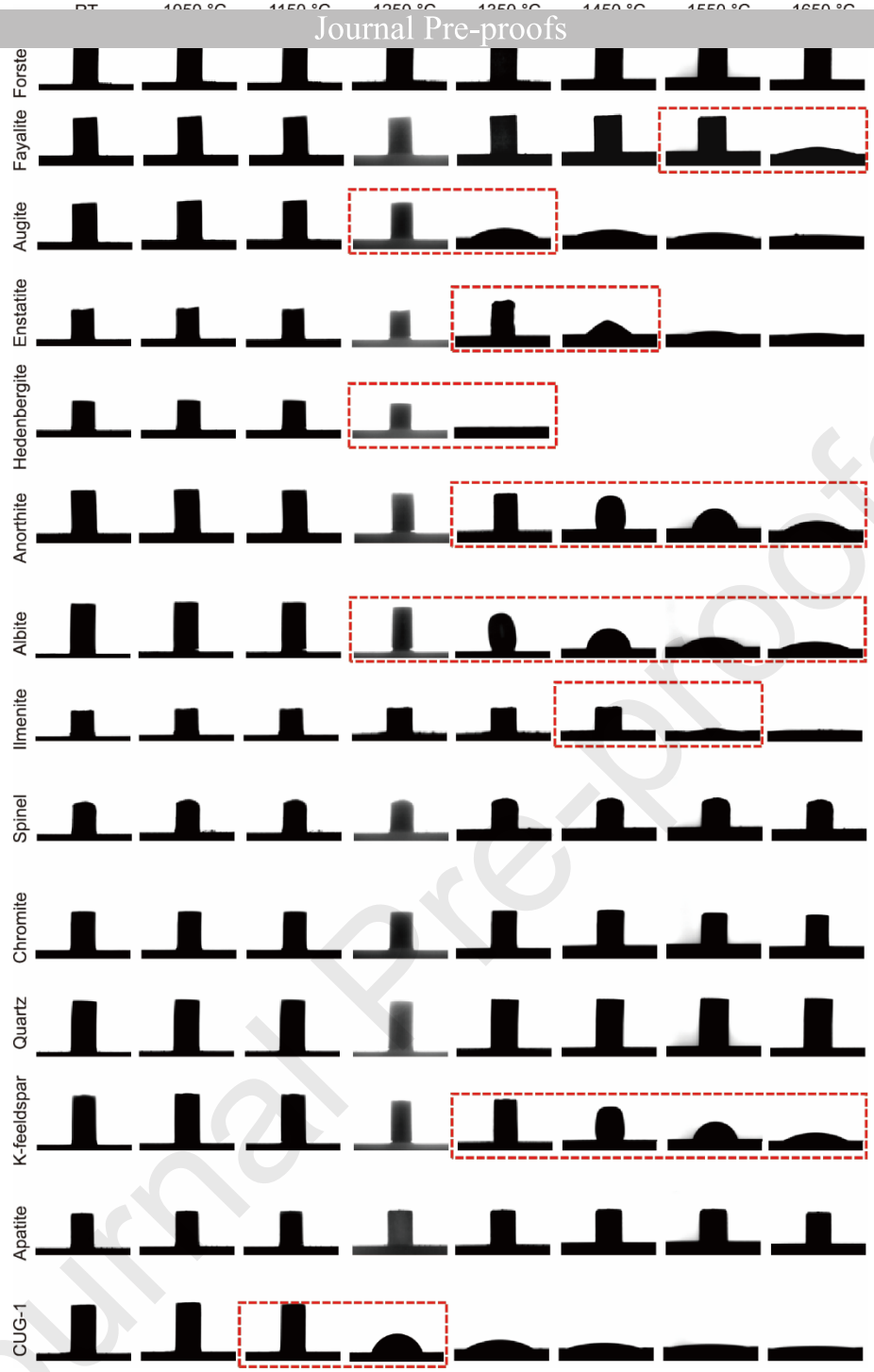


Fig.5 The heating and melting process of minerals.

Fig. S5 shows the solar radiation absorption of the minerals. Solar radiation absorptivity ranged from 638 $W \cdot m^{-2}$ (anorthite) to 1229 $W \cdot m^{-2}$ (ilmenite). Minerals with high iron and titanium content (ilmenite, chromite, enstatite) clustered at the high-absorptivity end, while the iron-poor, aluminum-rich feldspars (anorthite, albite) exhibited the lowest values. This trend is consistent with the d–d electronic transitions of transition metal cations, which broaden the absorption spectrum across the solar wavelength range.

The above analysis demonstrates that the fifteen minerals exhibit highly heterogeneous thermophysical profiles, with no single mineral excelling across all parameters simultaneously. This heterogeneity, combined with the process-dependent relevance of each parameter, necessitates a systematic multi-criteria evaluation framework to quantify mineral suitability for each specific manufacturing process.

3.2 Analysis of the influence of composition on the process

Three independent experts constructed pairwise comparison matrices for each process (the individual matrices are provided in Appendix A Tables S5–S13). These matrices were fused via geometric mean, and the resulting combined matrices for HPS,

MWS, and SLM are presented in Figs. 6(a)–(c), respectively. All three fused matrices satisfied the consistency requirement (CR[illegible]from the measured data, and the final combined weights were obtained through multiplicative normalization, as compared in Figs. 7(a)–(c).

The combined weight distributions differ significantly across the three processes. In HPS, κ received the highest combined weight (0.337), followed by η (0.219) and T_s (0.185), reflecting the dominant role of heat conduction and liquid-phase flow in pressure-assisted sintering. In MWS, tan δ accounted for 57.3% of the total weight, exceeding the second-ranked parameter (κ = 0.167) by a factor of 3.4. Both Fuzzy-AHP (0.360) and entropy weighting (0.271) assigned first rank to tan δ, and the multiplicative combination amplified this consensus. In SLM, α_{solar} ranked first (0.330), followed by γ (0.181) and η (0.170). The relatively high weight of γ in SLM, compared to HPS (0.072) and MWS (0.029), is attributed to the sensitivity of melt pool stability and intertrack bonding to surface tension during laser processing.

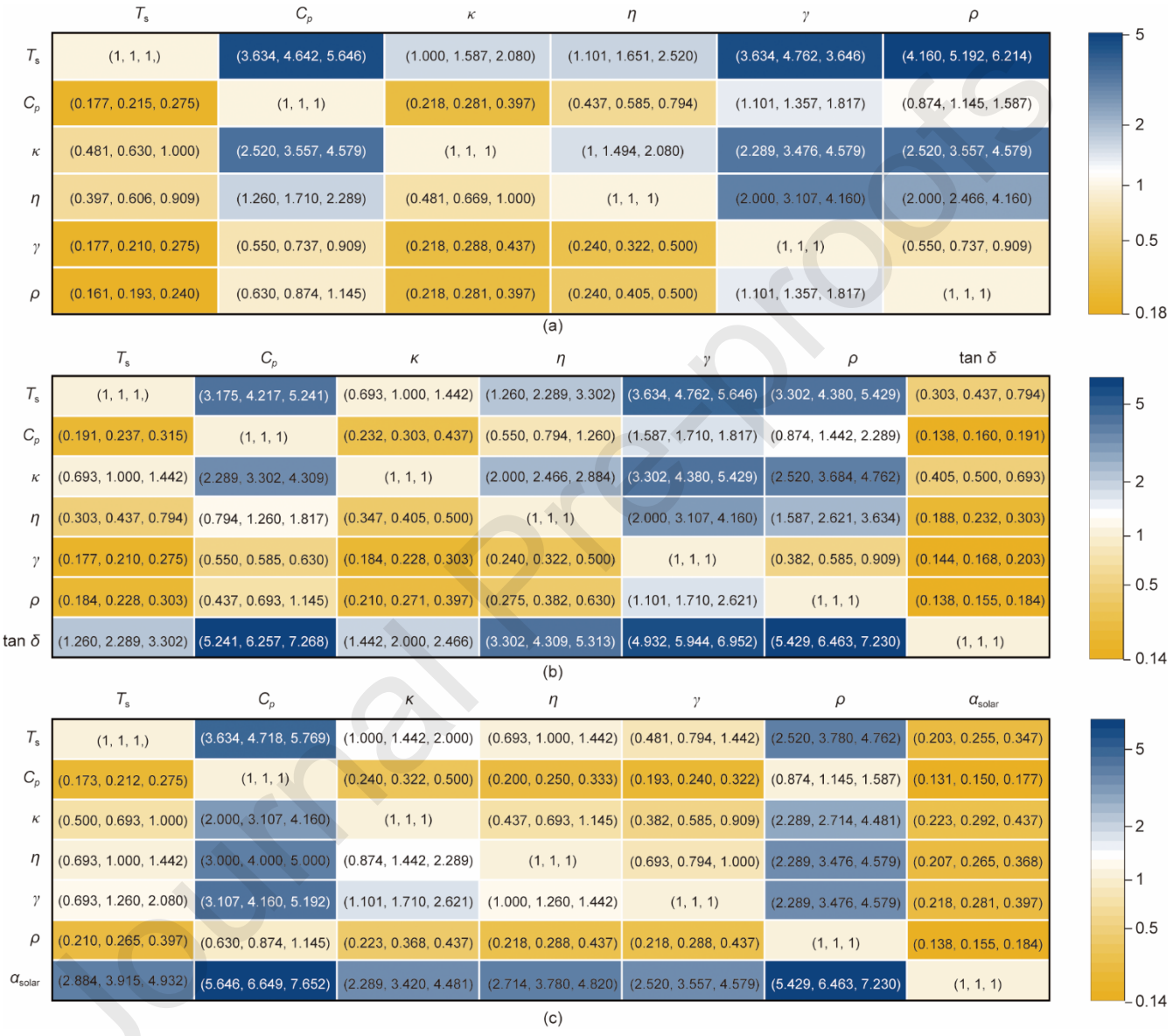


Fig.6 Fused Fuzzy-AHP pairwise comparison matrices for (a) HPS, (b) MWS, and (c) SLM. Each cell contains the triangular fuzzy number (*l*, *m*, *u*) (where *l*, *m*, and *u* represent the lower, modal, and upper bounds of the triangular fuzzy number, respectively) obtained by geometric mean fusion of three independent expert judgments. Color intensity represents the defuzzified *m*-value.

It is noteworthy that T_s received the highest Fuzzy-AHP weight in HPS (0.350) but the lowest entropy weight across all three processes (0.080). This discrepancy arises from the limited dispersion of T_s values among the ten ranked minerals, which reduces its information content in the entropy framework. The multiplicative normalization appropriately reconciles this mismatch, yielding a moderate combined weight that reflects both theoretical importance and practical discriminating power.

The TOPSIS closeness coefficients (C_i) and VIKOR compromise indices ($1 - Q_i$) are presented in Figs. 7(d)–(f). The principal results are summarized below. Ilmenite ranked first in all three processes (C_i = 0.890, 0.976, and 0.780 for HPS, MWS, and SLM, respectively), representing the only mineral to achieve top ranking across all evaluated manufacturing techniques. This universal superiority is attributed to its simultaneously favorable values in multiple high-weight parameters: tan δ = 0.146 (highest), α_{solar}=1229 W·m^{-2} (highest), κ = 0.584 W·(m·°C)$^{-1}$, log η = −1.41 (lowest), and ρ = 4.72 g·cm^{-3} (highest). The MWS ranking exhibited a pronounced hierarchical gap: Ilmenite (C_i = 0.976) exceeded the second-ranked

Journal Pre-proofs

enstatite (C_i = 0.176) by a factor of 5.5. This separation is a direct consequence of the tan δ-dominated weight structure com…xene group (enstatite, hedenbergite, augite) consistently occupied the second through fourth positions in HPS and the second through fourth positions in SLM, owing to their combination of moderate-to-high κ (0.29–0.47 W·(m·°C)$^{-1}$), low η (log η < 0), and intermediate T_s (1264–1420 °C). The feldspar group (anorthite, albite, K-feldspar) ranked in the bottom three positions for all three processes, with K-feldspar recording the lowest C_i values in HPS (0.144) and MWS (0.048). The consistently low ranking of feldspars is attributed to their high melt viscosity (log η > 2.4), low thermal conductivity (κ < 0.27 W·(m·°C)$^{-1}$), and low dielectric loss (tan δ < 0.031).

CUG-1A ranked 5th (HPS), 7th (MWS), and 6th (SLM), occupying a mid-range position consistent with its compositional representation of bulk lunar regolith. This positioning provides a natural baseline for the gradient blending validation described in Section 3.3. A process-dependent ranking reversal was observed for fayalite, which ranked 7th in HPS and 5th in MWS but dropped to last place (10th) in SLM. This reversal originates from the opposite direction assignments of thermal conductivity across processes: κ is classified as benefit-type in HPS and MWS, where higher conductivity promotes uniform heat distribution throughout the compact, but as cost-type in SLM, where lower conductivity is preferred to concentrate laser energy within the melt pool and prevent lateral heat dissipation. Fayalite possesses the highest κ in the dataset (0.651 W · (m·°C)$^{-1}$), which facilitates densification under conductive and volumetric heating modes but becomes a critical disadvantage under localized laser irradiation. This case illustrates that mineral suitability cannot be assessed in a process-independent manner and underscores the necessity of the process-specific weighting approach adopted in this study.

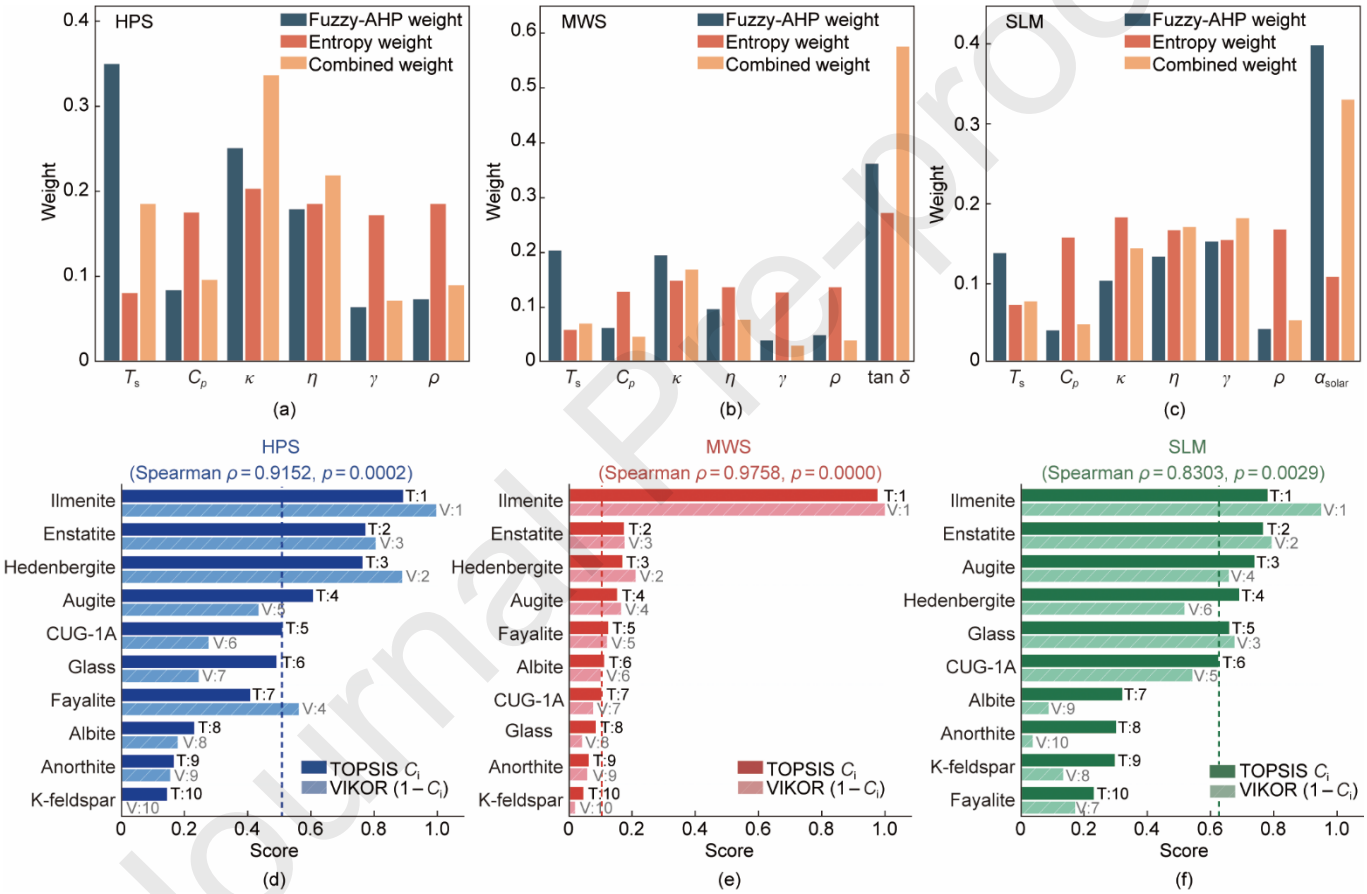


Fig.7 Process-specific weight analysis and mineral suitability ranking. (a–c) Comparison of Fuzzy-AHP, entropy, and combined weights for (a) HPS, (b) MWS, and (c) SLM. (d–f) TOPSIS closeness coefficients and VIKOR compromise scores for ten minerals, sorted by TOPSIS ranking. Spearman rank correlation coefficients between the two methods are annotated.

Monte Carlo simulation was performed to assess ranking stability under weight uncertainty. The combined weight vector was subjected to ±20% normal perturbation over 10 000 TOPSIS iterations per process. The resulting ranking distributions are shown in Figs. 8(a)–(c). Of the 30 mineral-process combinations, 28 exhibited σ < 1.0. The two exceptions were fayalite in HPS (σ = 1.01) and MWS (σ = 1.04), both marginally exceeding the threshold. The 95% confidence intervals confirm that the top three and bottom two minerals in each process maintained their positions throughout all perturbation scenarios. SLM exhibited the highest stability, with σ < 1.0 for all ten minerals. The VIKOR v-parameter was varied from 0.3 to 0.7 to evaluate ranking sensitivity to the decision strategy (Figs. 8(d)–(f)). In HPS and MWS, 9 of 10 minerals exhibited ranking fluctuations ≤ 1 position across the entire v range. In SLM, all ten minerals maintained constant rankings, producing perfectly horizontal lines. The sole source of variation was glass, which shifted by two positions at boundary v values in HPS and MWS.

Journal Pre-proofs

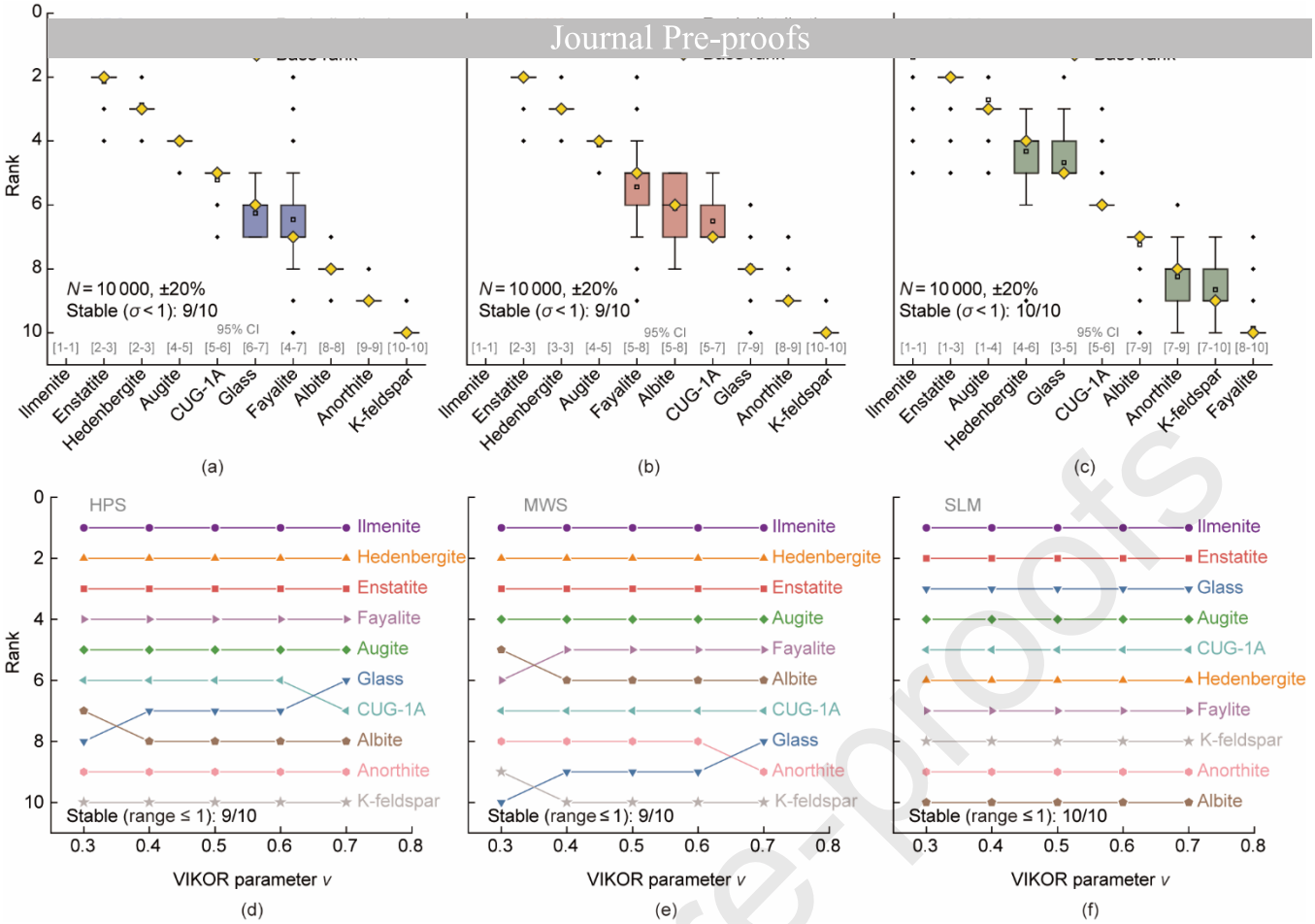


Fig.8 Sensitivity analysis of mineral rankings. (a–c) Monte Carlo simulation results (N = 10 000, ±20% weight perturbation): Box plots show ranking distributions with base ranks and 95% confidence intervals. (a) HPS, (b) MWS, and (c) SLM. (d–f) VIKOR v-parameter sensitivity (v = 0.3–0.7): ranking trajectories for each mineral across decision strategy preferences. (d) HPS, (e) MWS, and (f) SLM.

The convergent results from TOPSIS–VIKOR cross-validation, Monte Carlo weight perturbation, and VIKOR v-parameter analysis collectively demonstrate that the mineral suitability rankings are robust against algorithm selection, weight uncertainty, and decision strategy variation. The overall mineral-process suitability landscape is summarized in Fig. 9, where the color-coded matrix enables direct visual comparison across all mineral-process combinations.

To further test the effect of systematic preference variation, an additional preference-scenario sensitivity analysis was performed, and the results are shown in Appendix A Fig. S6. Compared with the original combined-weight ranking, strengthening or weakening the dominant process-controlling parameter did not alter the main engineering conclusions. For HPS and MWS, ilmenite remained ranked first in all scenarios. For SLM, although the internal order among the top-ranked minerals changed slightly when the α_{solar} weight was weakened, the favorable group consistently consisted of ilmenite and pyroxene-group minerals. Feldspar-group minerals remained in the unfavorable range under all scenarios. The scenario rankings remained highly correlated with the original combined-weight ranking, with Spearman correlation coefficients of 0.964–0.988 for HPS, 0.964–0.976 for MWS, and 0.952–0.976 for SLM, indicating that the principal ranking conclusions are robust to systematic variation in dominant-parameter preference.

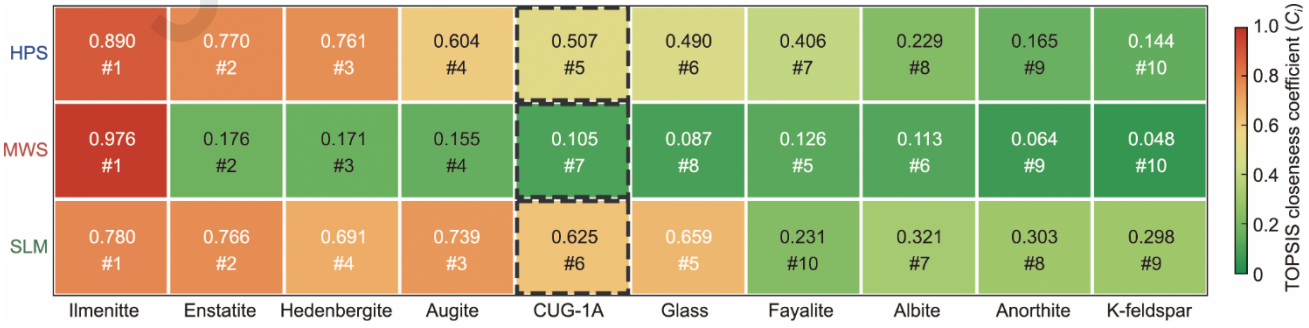


Fig.9 Mineral-process suitability matrix. Each cell displays the TOPSIS closeness coefficient (C_i) and ranking for a given mineral-process combination. Color scale: red indicates high suitability, green indicates low suitability. CUG-1A (dashed outline) serves as the baseline lunar regolith simulant.

Journal Pre-proofs

3.3.1 Hot-press sintering

For HPS, gradient blending experiments were conducted using ilmenite (ranked 1st by TOPSIS) and anorthite (ranked 9th) as representative favorable and unfavorable minerals, respectively. Fig. 10 presents the five hot-press sintered lunar regolith samples, arranged from top to bottom as follows: 80% CUG-1A + 20% ilmenite, 90% CUG-1A + 10% ilmenite, 100% CUG-1A, 90% CUG-1A + 10% anorthite, and 80% CUG-1A + 20% anorthite. All samples are cylindrical with a diameter of 10 mm and a height of 20 mm.

Variations in mineral composition exerted a pronounced influence on both macroscopic appearance and microstructure. Macroscopically, the ilmenite-enriched samples (20%Ilm and 10%Ilm) exhibited darker surface coloration compared to the CUG-1A baseline, whereas the anorthite-enriched samples (10%An and 20%An) displayed a progressive shift toward light gray with increasing anorthite content. Figs. 10(a-i)-(e-i) present backscattered electron (BSE) images of the sintered sample cross-sections. The micro-area elemental distributions were analyzed by energy-dispersive spectroscopy (EDS) mapping, and the results are provided in Appendix A Figs. S7–S11. Metallic iron (Fe^0) particles were observed throughout all samples, originating from the thermal decomposition of mafic silicates during high-temperature sintering, which produces a dispersed metallic iron phase [61]. The presence of this phase contributes to the observed color variation and may additionally influence the mechanical and electromagnetic properties of the sintered bodies [62–64].

The elemental composition analysis is presented in Fig. 11(a). The relative contents of Fe and Ti decreased systematically with decreasing ilmenite content and increasing anorthite content, consistent with the designed compositional gradient. The relative density of each sample was determined from BSE images using ImageJ software: Pore regions were identified as the lowest-contrast areas, and the densification was calculated from the extracted porosity fraction. As shown in Fig. 11(b), the relative densities of 20%Ilm, 10%Ilm, CUG-1A, 10%An, and 20%An were 85.212%, 82.177%, 77.711%, 75.926%, and 73.374%, respectively, exhibiting a monotonic decreasing trend consistent with the TOPSIS-predicted suitability ranking. This result confirms that ilmenite addition enhances HPS performance, whereas anorthite addition degrades it.

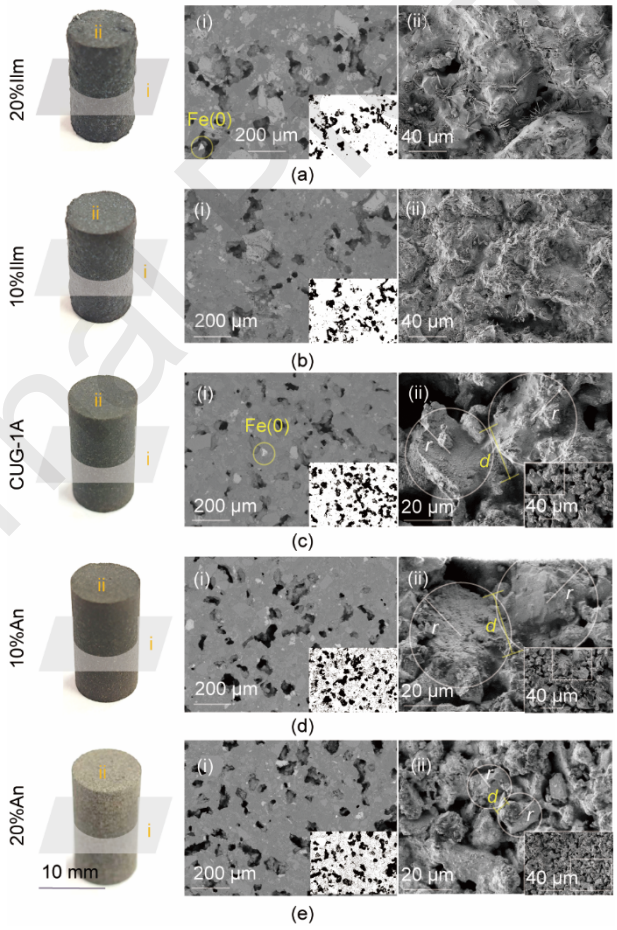


Fig.10 Appearance, internal pore structure, and surface morphology of hot-press sintered samples.

According to the spherical sintering model proposed by Kuczynski [65], the degree or rate of sintering is generally expressed in terms of the sintering shrinkage, as shown in Eq. (5).

Journal Pre-proofs

$$\text{Sintering shrinkage} = \frac{\Delta L}{L_0} = \frac{(r_1 + r_2) - d}{(2r_1) \times (2r_2)}$$

where ΔL denotes the reduced distance between the two spheres; L_0 is the initial distance between the two balls; d represents the diameter of sintering neck (μm), and r_1 and r_2 are the radius of powder particles (μm).

The fracture surfaces of the ilmenite-enriched samples (20%Ilm and 10%Ilm) exhibited a continuous morphology with no discernible original particle boundaries, indicating a high degree of sintering (Figs. 10(a-ii) and (b-ii)). In contrast, the baseline and anorthite-enriched samples (Figs. 10(c-ii)–(e-ii)) retained distinct particle outlines with visible sintering necks between adjacent particles. To quantify the sintering degree, multiple particle pairs were selected from each sample, and the particle radius (r) and sintering neck radius (d) were measured. The sintering degree was calculated using Eq. (5), with the results presented in Fig. 11(b). The sintering degree of the baseline CUG-1A sample was 0.096, while the 20%An sample exhibited the lowest value of 0.041. These measurements demonstrate that decreasing ilmenite content or increasing anorthite content leads to a significant reduction in sintering degree, which in turn governs the densification and thermo-mechanical performance of the fabricated components.

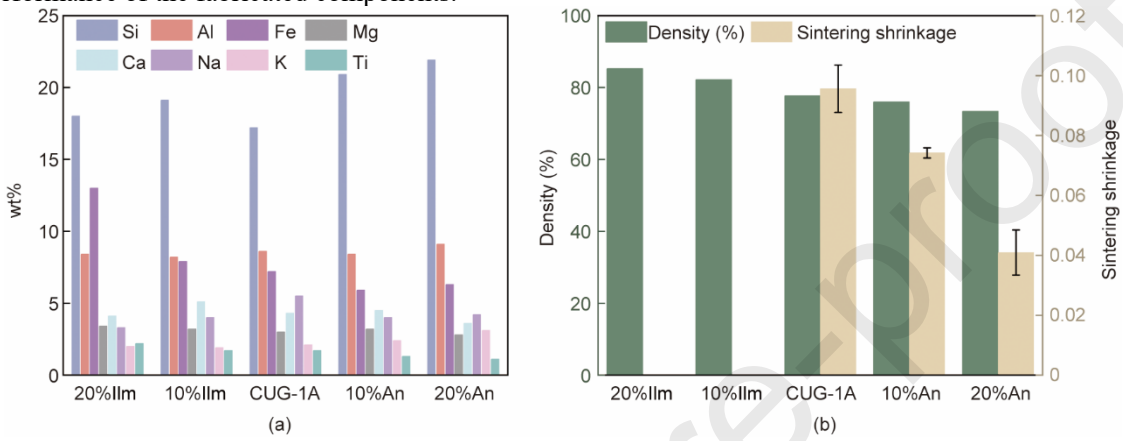


Fig.11 (a) The element content of hot-press sintered samples with different mineral ratios. (b) Analysis of density and sintering shrinkage of hot-pressed sintered samples with different mineral ratios.

3.3.2 Microwave sintering

For MWS, gradient blending experiments were conducted using ilmenite (ranked 1st by TOPSIS) and K-feldspar (ranked 10th) as representative favorable and unfavorable minerals, respectively. Fig. 12 presents the five microwave-sintered lunar regolith samples. All samples were sintered in quartz crucibles under microwave irradiation at 2.45 GHz.

The macroscopic photographs and computed tomography (CT) cross-sections (leftmost columns) reveal a clear compositional dependence of sintering quality. The ilmenite-enriched samples (20%Ilm and 10%Ilm) exhibited uniform dark coloration and dense, homogeneous CT cross-sections with minimal porosity. In contrast, the K-feldspar-enriched samples (10%Kfs and 20%Kfs) showed lighter surface coloration, and the CT images reveal progressively increasing internal porosity and crack formation, particularly in the 20%Kfs sample, which displayed a fragmented cross-section with significant structural defects.

Journal Pre-proofs

Journal Pre-proofs

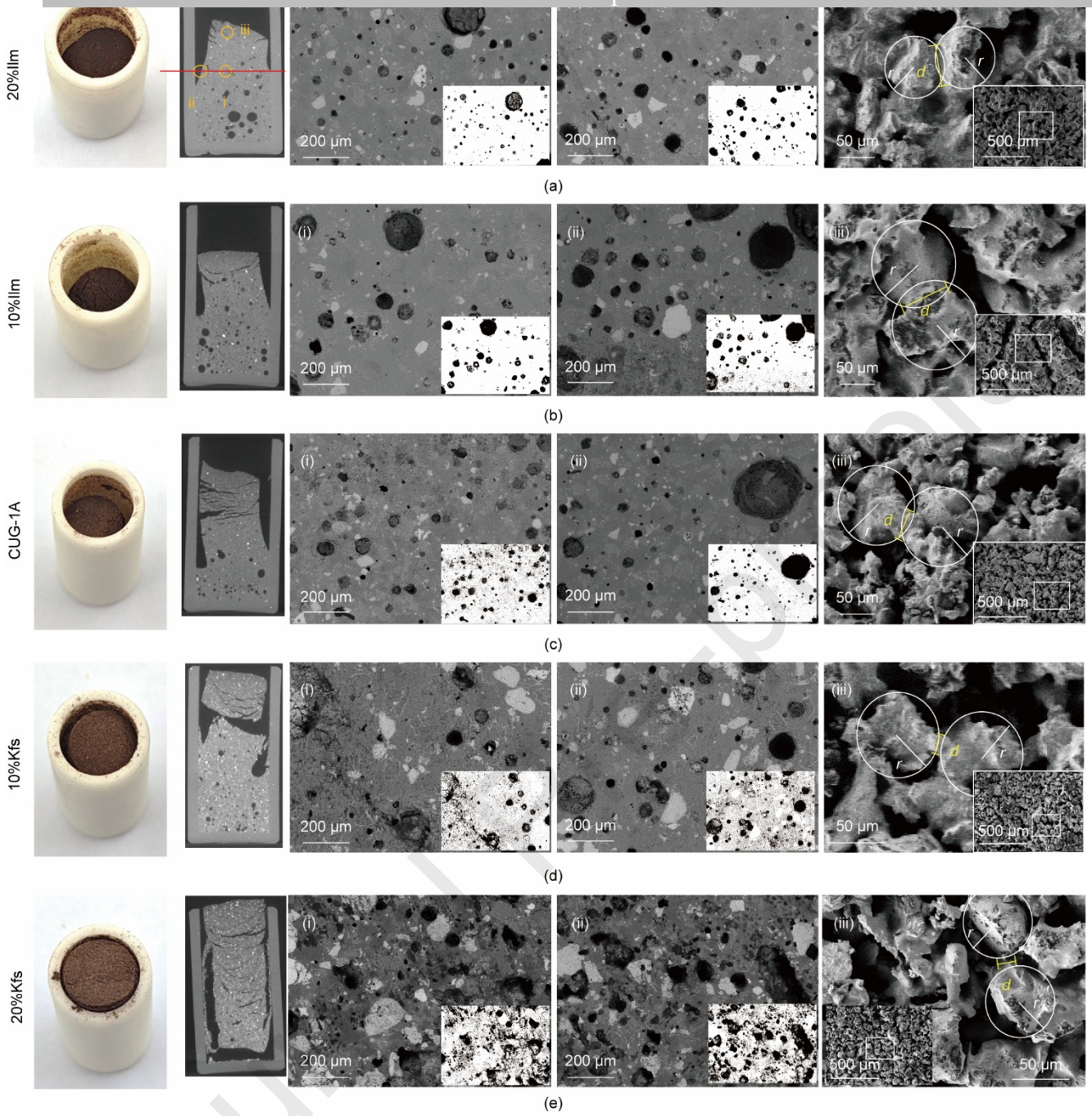


Fig.12 Microwave-sintered samples, CT images, and surface and internal microstructures of the microwave sintered samples. (a) 80% CUG-1A + 20% ilmenite, (b) 90% CUG-1A + 10% ilmenite, (c) 100% CUG-1A, (d) 90% CUG-1A + 10% K-feldspar, and (e) 80% CUG-1A + 20% K-feldspar. ((a-i)–(e-i)) Backscattered image and pore structure analysis of sample surface. ((a-ii)–(e-ii)) Backscattering image and pore structure analysis inside the sample. ((a-iii)–(e-iii)) Microstructure of the sample surface. Ilm: ilmenite. Kfs: K-feldspar.

The internal and external microstructures were examined by BSE imaging (columns 2 and 3). Pore regions were extracted from the BSE images (insets) for quantitative densification analysis. A systematic increase in pore fraction was observed from 20%Ilm to 20%Kfs, consistent with the macroscopic observations. A comparison between the internal (column 2) and external (column 3) BSE images reveals that the internal porosity was consistently lower than the external porosity across all five samples. This inside-out densification gradient is characteristic of MWS: unlike conventional heating where thermal energy is conducted inward from the surface, microwave radiation penetrates the bulk and induces volumetric heating, resulting in preferential densification of the sample interior. This observation provides direct microstructural evidence for the volumetric heating mechanism of MWS and further highlights the critical role of tan δ in governing the spatial uniformity of energy deposition. As shown in Fig. 13, the relative densities within the samples determined from BSE image analysis were 93.562% (20%Ilm), 89.736% (10%Ilm), 85.436% (CUG-1A), 83.145% (10%Kfs), and 75.821% (20%Kfs), confirming a monotonic decreasing trend in agreement with the TOPSIS-predicted suitability ranking. Notably, the MWS process exhibited the largest densification response among the three processes: The difference between 20%Ilm and 20%Kfs reached 17.7 percentage points, reflecting the dominant influence of tan δ on microwave energy coupling efficiency. Ilmenite, with tan $\delta = 0.146$ (4.6×

higher than any other mineral), dramatically enhances volumetric heating and thus densification, whereas K-feldspar (tan δ = 0.02

Journal Pre-proofs

The external surface morphologies are presented in the rightmost column (Figs.12(a-iii)–(e-iii)). The ilmenite-enriched samples exhibited well-developed sintering necks between adjacent particles, with the neck diameter (*d*) approaching the particle radius (*r*), indicating near-complete inter-particle bonding. The CUG-1A sample (Fig. 12(c-iii)) showed smaller but clearly formed sintering necks. In the K-feldspar-enriched samples, the sintering necks were progressively thinner (Fig. 12(d-iii) or barely discernible (Fig. 12(e-iii), and individual particle boundaries remained sharply defined, indicating insufficient inter-particle fusion. The sintering degree, which was calculated by Eq. (5) and shown in Fig. 13, was 0.0855 (20%Ilm), 0.0756 (10%Ilm), 0.0270 (CUG-1A), 0.0110 (10%Kfs), and 0.0057 (20%Kfs). This monotonic decrease is consistent with the TOPSIS ranking and further corroborates the conclusion that ilmenite is the most favorable mineral for microwave sintering, while K-feldspar is the least favorable.

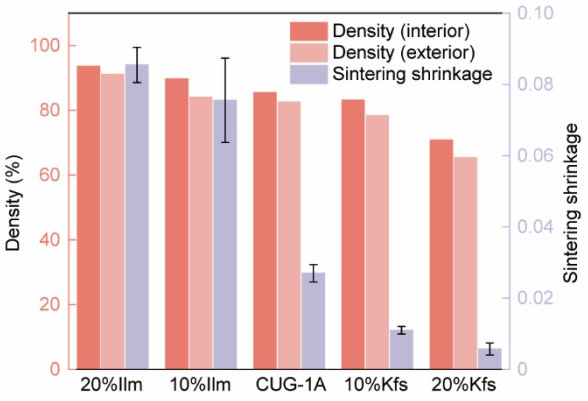


Fig.13 Pore analysis of internal and surface of microwave sintered samples and sintering shrinkage rate analysis.

3.3.3 Selective laser melting

For SLM, gradient blending experiments were conducted using ilmenite (ranked 1st by TOPSIS) and albite (ranked 7th) as representative favorable and unfavorable minerals, respectively. Fig. 14(a) presents the macroscopic photographs of the five SLM-fabricated samples: 80% CUG-1A + 20% ilmenite, 90% CUG-1A + 10% ilmenite, 100% CUG-1A, 90% CUG-1A + 10% albite, and 80% CUG-1A + 20% albite. All samples were fabricated as multi-layer cubic specimens on a substrate.

Macroscopically, the ilmenite-enriched samples exhibited relatively smooth, uniform top surfaces, whereas the albite-enriched samples displayed noticeably rougher and more irregular surface textures. This qualitative trend was quantified by the areal surface roughness parameter *Sa*, defined as the arithmetic mean deviation of the surface height from the mean plane. For each sample, 18 measurement points were uniformly distributed across the top surface, and the resulting *Sa* values are presented as box plots in Fig. 14(b).

$$Sa = \frac{1}{A}\iint_{A} |Z(x,y)|\mathrm{d}x\mathrm{d}y$$

where A is the area of the evaluated surface, $Z(x,y)$ is the surface height relative to the mean plane at position (x,y), and x and y are the in-plane Cartesian coordinates. The mean *Sa* values increased monotonically from 20%Ilm (about 20 μm) through the CUG -1A (~25 μm) to 20%Ab (~40 μm), confirming that ilmenite addition improves SLM surface quality while albite addition degrades it. The box plot distributions further reveal that the 20%Ilm and 10%Ilm samples exhibited the narrowest *Sa* distributions, indicating not only lower absolute roughness but also greater spatial uniformity across the scanned surface. In contrast, the B-20 sample showed a broad *Sa* distribution with several outliers exceeding 80 μm, suggesting localized balling or incomplete melting events.

The three-dimensional microstructure was characterized by micro-CT, and the reconstructed surface morphology, cross-section, and extracted pore networks for each sample are presented in Fig. 14(c)–(g). The porosity values, determined from the segmented CT volumes, were 0.113 (20%Ilm), 0.124 (10%Ilm), 0.128 (CUG-1A), 0.139 (10%Ab), and 0.140 (20%Ab), exhibiting a monotonic increase from the ilmenite-enriched to the albite-enriched compositions. The cross-sectional reconstructions reveal that the 20%Ilm sample possessed the most uniform melt track morphology with minimal inter-track voids, while the 20%Ab sample exhibited irregular track boundaries and interconnected pore networks.

The superior SLM performance of ilmenite-enriched compositions is attributed to two synergistic effects. First, ilmenite possesses the highest solar absorptivity in the dataset (α_{solar} = 1229 W·m^{-2}), which enhances laser energy absorption and promotes complete melting of the powder bed. Second, ilmenite's low melt viscosity (log η = −1.41) facilitates melt flow and inter-track wetting, reducing the incidence of balling defects. Conversely, albite suffers from low α_{solar} (706 W·m^{-2}) and high melt viscosity (log η = 2.40), both of which impair melt pool formation and spreading.

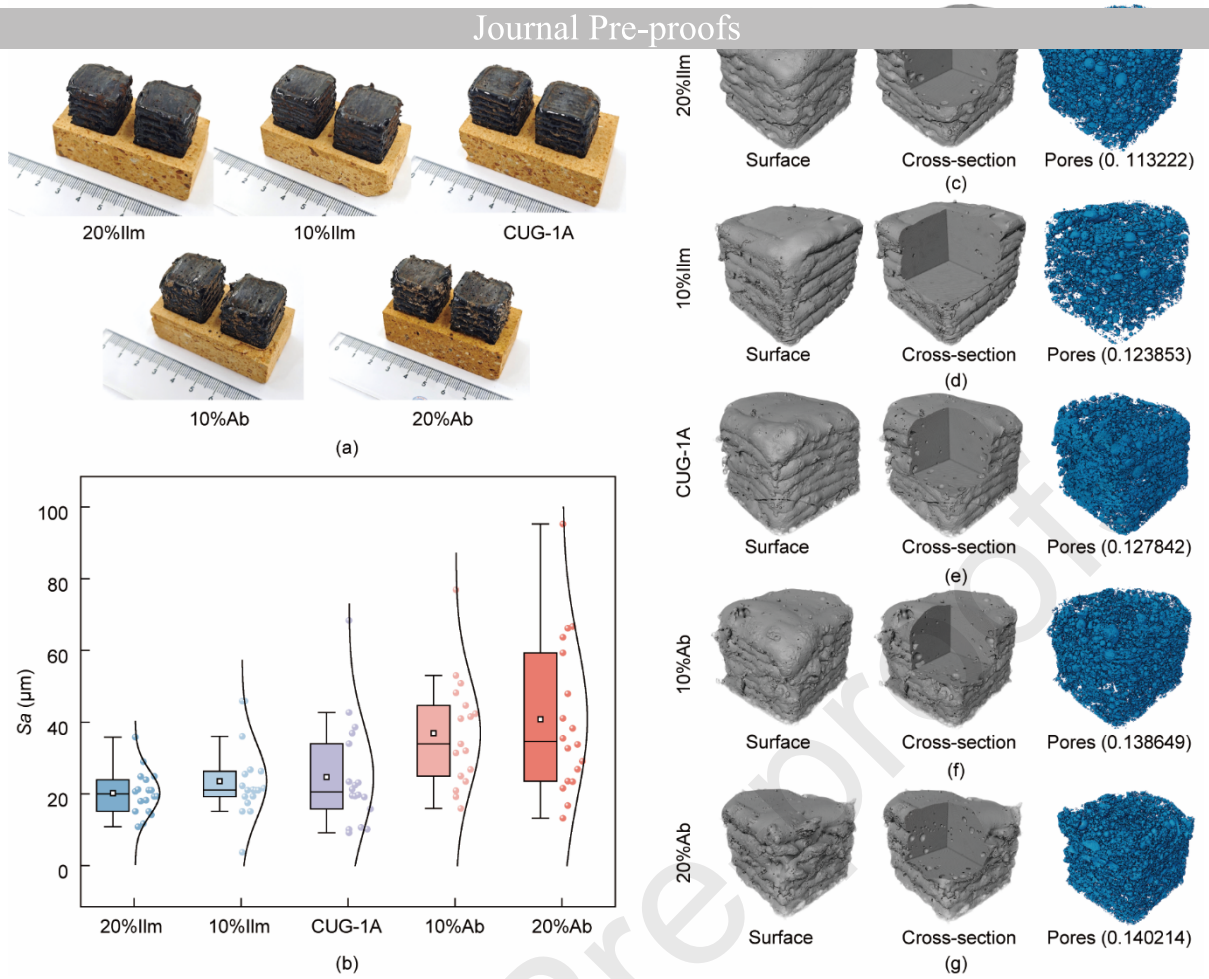


Fig.14 (a) Selective laser melted samples. Ab: albite. (b) Surface roughness analysis of SLM formed samples. (c–g) The CT structure of SLM formed samples: (c)80% CUG-1A + 20% ilmenite, (d) 90% CUG-1A + 10% ilmenite, (e) 100% CUG-1A, (f) 90% CUG-1A + 10% albite, and (g) 80% CUG-1A + 20% albite. The surface, cross-section, and pore structure of the samples are shown from left to right.

4. Discussion

4.1 Analysis of densification

To evaluate whether the TOPSIS-predicted rankings translate into measurable performance differences, the experimental results were correlated with the predicted scores using a normalized representation: ΔC_i (TOPSIS score change from baseline) versus the relative change in the experimental metric. This normalization removes absolute differences in baseline performance across the three processes and enables direct cross-process comparison.

Fig. 15(a) presents the cross-process correlation between ΔC_i and relative density change for all gradient blending configurations. All twelve non-baseline data points fall in the first and third quadrants—no composition predicted to improve performance degraded it, and vice versa. The cross-process Pearson correlation is $r = 0.788$ ($p = 0.002$) and the Spearman correlation is $\rho = 0.825$ ($p = 0.001$). Within each process, Spearman's $\rho = 1.000$, indicating perfect rank-order agreement with the TOPSIS prediction. These results demonstrate that the framework is valid both in ordering minerals correctly and in approximating the magnitude of performance change.

The process-specific microstructural validations (Fig. 15(b)–(d)) further corroborate this conclusion at the microscopic scale. For HPS sintering degree (Fig. 15(b)), only two non-baseline data points were available because the ilmenite-enriched samples achieved such complete inter-particle fusion that sintering necks could not be measured—itself qualitative evidence of superior performance. The two available points follow a consistent downward trend with decreasing ΔC_i. For MWS sintering degree (Fig. 15(c)), the Spearman correlation is $\rho = 1.000$ ($p < 0.001$) and the Pearson correlation is $r = 0.949$ ($p = 0.051$, $N = 4$). The response was notably asymmetric: Ilmenite addition improved the sintering degree by 217% relative to the baseline, whereas K-feldspar addition reduced it by 79%. This asymmetry reflects the nonlinear relationship between tan δ and microwave heating efficiency, suggesting that even modest ilmenite enrichment can yield substantial improvements in microwave sintering quality. For SLM surface roughness improvement (Fig. 15(d)), the strongest linear correlation was observed ($r = 0.990$, $p = 0.010$; $\rho = 1.000$, $p < 0.001$), attributed to the synergistic effects of ilmenite's high solar absorptivity and low melt viscosity on melt pool formation and spreading.

Across all available validation metrics, every Spearman correlation equals 1.000 and every Pearson correlation exceeds 0.78, providing converging evidence from both macroscopic and microscopic scales that the proposed framework captures the essential physics governing mineral-process interactions in lunar ISRU manufacturing.

Journal Pre-proofs

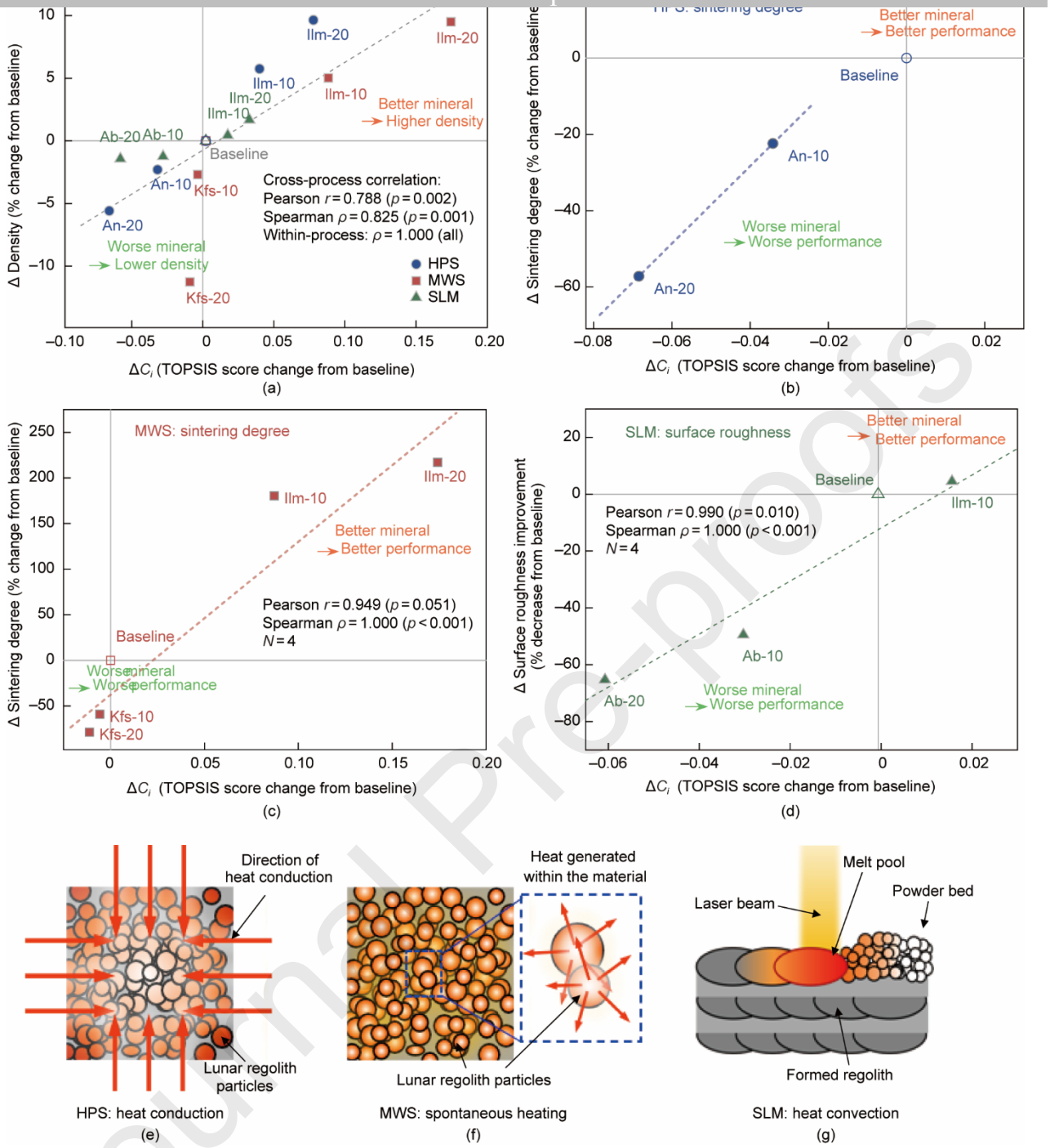


Fig.15 Experimental validation and process mechanism analysis. (a) Cross-process correlation between TOPSIS-predicted score change (ΔC_i) and experimental relative density change (ΔDensity) for all three processes. (b–d) Process-specific correlations between ΔC_i and microstructural parameters: (b) HPS sintering degree, (c) MWS sintering degree, and (d) SLM surface roughness improvement. Dashed lines represent linear regression fits. (e–g) Schematic illustrations of the dominant heat transfer mechanisms: (e) HPS—heat conduction from die walls through the raw powder, (f) MWS—spontaneous volumetric heating via dielectric energy dissipation, and (g) SLM—localized melting by laser beam with heat convection in the melt pool.

The distinct weight structures and ranking patterns identified in Section 3.2 originate from fundamental differences in the heat transfer mechanisms governing the three manufacturing processes, as illustrated schematically in Figs. 15(e)–(g).

In HPS (Fig. 15(e)), heat is supplied externally through resistive heating elements and conducted inward through the die walls into the powder compact. The densification rate is therefore governed by the efficiency of heat conduction through the particle network, which directly explains the dominance of thermal conductivity ($\kappa = 0.337$) in the combined weight structure. Minerals with high κ (e.g., ilmenite, 0.584 $W\cdot(m\cdot°C)^{-1}$; fayalite, 0.651 $W\cdot(m\cdot°C)^{-1}$) facilitate rapid and uniform temperature distribution throughout the compact, enabling homogeneous liquid-phase formation and pore elimination under the applied uniaxial pressure. Conversely, minerals with low κ (e.g., K-feldspar, 0.209 $W\cdot(m\cdot°C)^{-1}$) create thermal gradients that lead to non-uniform sintering, with the compact interior remaining under-sintered relative to the surface. The secondary role of melt

viscosity (η = 0.219) reflects the pressure-assisted densification mechanism: under sustained mechanical load, a low-viscosity liqu

Journal Pre-proofs

In MWS (Fig. 15(f)), heating occurs spontaneously within the material volume through dielectric energy dissipation at 2.45 GHz, without an external thermal gradient. The rate of internal heat generation is proportional to the dielectric loss tangent (tan δ), which explains its extreme weight dominance (0.573). This volumetric heating mechanism produces a fundamentally different temperature profile compared to HPS: The sample interior heats preferentially, while the surface loses heat to the surrounding environment, resulting in an inverted thermal gradient. This is consistent with the microstructural observation that the internal porosity of MWS samples was systematically lower than the external porosity. Because ilmenite's tan δ (0.146) exceeds that of all other minerals by a factor of 4.6–9.9, its presence in the feedstock effectively determines whether the powder can couple with microwave radiation at all. The secondary importance of κ (0.167) in MWS reflects a different physical role than in HPS: here, higher κ helps redistribute the internally generated heat toward the cooler surface, reducing the inverted thermal gradient and promoting more uniform densification throughout the compact.

In SLM (Fig. 15(g)), a focused laser beam scans the powder bed surface, creating a localized melt pool that rapidly solidifies as the beam advances. The energy input is concentrated in a small area (~100 μm diameter), and the powder must absorb sufficient laser radiation to achieve complete melting within the brief interaction time. This explains the dominance of solar absorptivity (α_{solar}=0.330) in the SLM weight structure. Unlike HPS and MWS, where thermal conductivity is beneficial for distributing heat, in SLM high κ is detrimental: It causes rapid lateral heat dissipation away from the melt pool, reducing the peak temperature and potentially leading to incomplete melting—the physical basis for the cost-type assignment of κ in SLM and the consequent last-place ranking of fayalite (highest κ). The elevated weight of surface tension (γ = 0.181) in SLM, compared to the other two processes, is attributed to its governing role in melt pool dynamics: Appropriate surface tension promotes spherical melt pool formation and stable inter-track bonding, while insufficient surface tension leads to balling defects and irregular track morphology.

The three heating mechanisms thus define three distinct parameter hierarchies—κ-dominated (HPS), tan δ-dominated (MWS), and α_{solar} -dominated (SLM) —which propagate through the TOPSIS ranking to produce process-specific mineral suitability sequences. This coincidence is rooted in the Fe^{2+}–Ti^{4+} electronic configuration of ilmenite: The intervalence charge transfer (IVCT) between Fe^{2+} and Ti^{4+} produces broadband optical absorption across the visible-near-infrared spectrum [66,67], contributes to dielectric loss through electronic conduction at microwave frequencies [68,69], and the dense oxide crystal structure with mixed ionic-covalent bonding facilitates efficient phonon transport.

To further supplement the validation with a mechanical-performance metric, hardness testing was added, and the results are shown in Appendix Figs. S12 and S13. The hardness trends are consistent with the densification and defect analyses: Ilmenite-enriched samples generally showed higher hardness, whereas feldspar-enriched samples showed lower hardness. Specifically, hardness increased from 391.80 HV (An-20) to 507.31 HV (Ilm-20) for HPS, from 299.14 HV (Kfs-20) to 661.94 HV (Ilm-20) for MWS, and from 619.83 HV (Ab-20) to 698.45 HV (Ilm-20) for SLM. The positive monotonic relationship between hardness change and TOPSIS suitability change further supports the mineral-suitability ranking, although the hardness response should not be interpreted as a strict linear relationship because of local porosity and phase heterogeneity.

4.2 The prospect of future scenarios

The mineral suitability rankings established in this study have direct implications for the design of future lunar ISRU manufacturing systems. As illustrated conceptually in Fig. 16, the proposed framework suggests a paradigm shift from the current "use bulk regolith as-is" approach to a "beneficiate-then-manufacture" strategy, in which excavated lunar regolith is first subjected to mineral separation and then directed to the most compatible manufacturing process based on the enriched mineral composition.

The universal superiority of ilmenite across all three processes makes it a priority target for beneficiation. Ilmenite is strongly paramagnetic due to its Fe^{2+}–Ti^{4+} electronic structure, which makes it readily separable from the weakly magnetic silicate matrix by low-field magnetic separation—a technique that has already been demonstrated for lunar regolith simulants and Apollo samples. An ilmenite-enriched feedstock would simultaneously enhance microwave coupling (via high tan δ), laser absorption (via high α_{solar}), and sintering kinetics (via high κ and low η), regardless of which manufacturing process is subsequently employed. This process-agnostic advantage simplifies the logistics of a lunar manufacturing facility, as a single beneficiation step can serve multiple downstream processes.

The validation results further provide process-specific first-order engineering references for the "beneficiate-then-manufacture" strategy. Based on the linear fits summarized in Appendix A Eqs. (S5)–(S11) and Table S17, the HPS series shows that the 20 wt% ilmenite-enriched sample reached 85.2% relative density (RD), and reaching 90% relative density would require approximately 37 wt% ilmenite enrichment by first-order extrapolation, beyond the tested range. For MWS, if 90% relative density is used as a practical manufacturability reference threshold, the CUG-1A/mare-type feedstock requires approximately 10–11 wt% ilmenite enrichment, whereas feldspar-rich/highland-type feedstock may require approximately 20–30 wt% ilmenite enrichment equivalent. For SLM, 20 wt% ilmenite enrichment reduced CT porosity from 0.128 to 0.113 and lowered surface roughness from approximately 25 to 20 μm. These values should be interpreted as first-order estimates from controlled CUG-1A perturbation experiments, rather than universal thresholds for all multiphase lunar regolith.

The results also suggest process-specific beneficiation strategies for cases where ilmenite is scarce. For HPS and SLM, enrichment of the pyroxene fraction (enstatite, hedenbergite, augite) would provide substantial performance gains, as these minerals ranked 2nd–4th in both processes. Pyroxenes are denser than feldspars and can be partially concentrated by gravity

or centrifugal separation methods. Conversely, the results indicate that feldspar-rich regolith (characteristic of the lunar high[illegible]with access to mare basalts, which are inherently rich in ilmenite and pyroxene, would therefore be preferred from a manufacturing perspective.

The gradient blending experiments also suggest that TOPSIS closeness coefficients can be used as a first-order indicator for feedstock screening. In the present CUG-1A-based perturbation tests, mineral enrichment produced forming trends consistent with the predicted mineral suitability. However, this relationship should be regarded as an empirical trend within the tested composition range, rather than a universal linear mixing rule for real multiphase lunar regolith. Nonlinear effects such as eutectic melting, solid-solution formation, interfacial reactions, and glass-assisted liquid formation may alter the absolute forming response in more complex mineral assemblages.

In summary, this study establishes a quantitative link between lunar regolith mineralogy and ISRU manufacturing performance through a systematic Fuzzy-AHP + entropy + TOPSIS/VIKOR framework. The experimental validation confirms the predictive capability of the framework at both macroscopic and microscopic scales. The findings identify ilmenite as the universally optimal mineral for all three thermal manufacturing processes, recommend pyroxene enrichment as a secondary strategy, and highlight the unsuitability of feldspar-dominated feedstocks. These results provide actionable guidance for mineral beneficiation design, manufacturing process selection, and landing site evaluation in future lunar base construction programs.

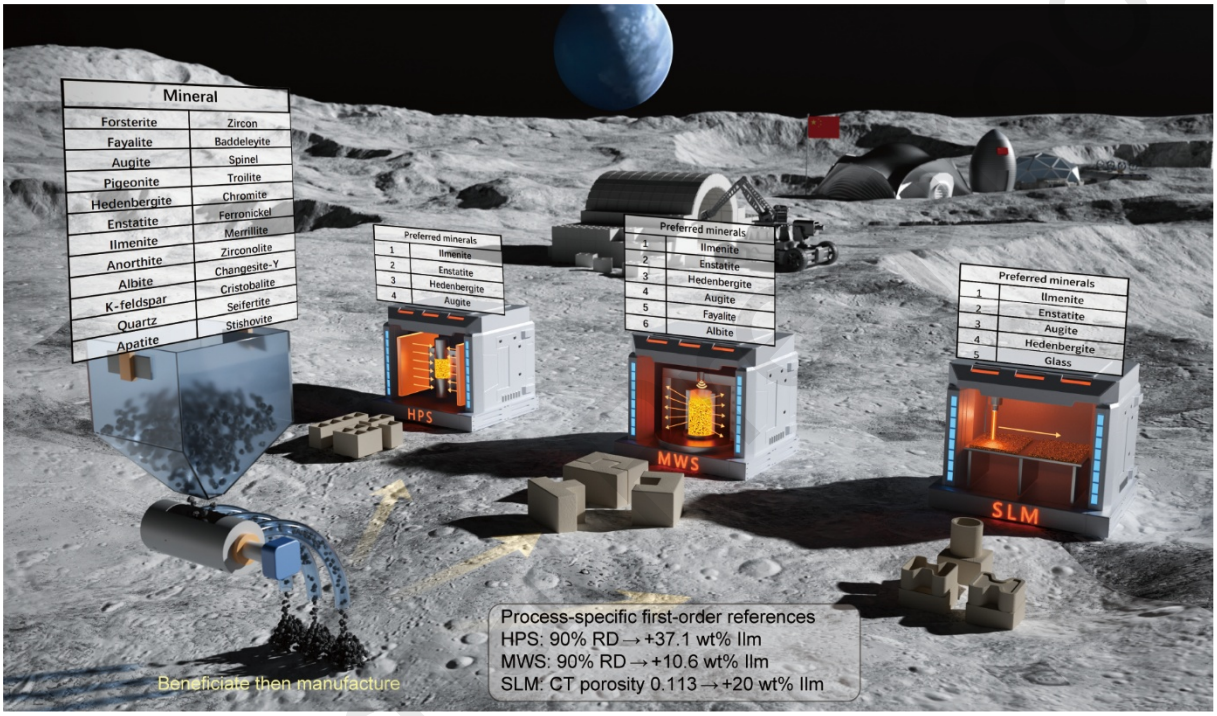


Fig. 16. Conceptual illustration of mineral-specific feedstock selection for lunar ISRU manufacturing. Excavated lunar regolith undergoes mineral beneficiation (e.g., magnetic separation) to produce process-optimized feedstocks, which are directed to three representative manufacturing techniques (HPS, MWS, and SLM) based on the mineral suitability rankings established in this study. The inset summarizes process-specific first-order engineering references derived from the CUG-1A perturbation experiments, including ilmenite enrichment thresholds for HPS and MWS and porosity/roughness improvement for SLM. The fabricated structural components are used for lunar base construction.

Several limitations should be acknowledged. First, the experimental conditions in this study do not fully reproduce the lunar surface environment. Although the HPS validation was conducted under a low pressure of 40 Pa, this is still much higher than the high-vacuum condition on the Moon, and the MWS, SLM, and part of the thermophysical characterization were performed under ground-based laboratory conditions. High vacuum and reduced gravity may affect heat transfer, powder packing, melt flow, and pore evolution, and therefore the present results should not be regarded as a final validation of lunar-surface manufacturing performance. Nevertheless, the purpose of this study is to establish a relative mineral-suitability ranking rather than absolute lunar process windows. Because the key ranking parameters are mainly governed by mineral crystal structure and major-element chemistry, these environmental effects are expected to influence absolute forming quality more strongly than the relative order among minerals. Validation under high-vacuum and reduced-gravity conditions remains necessary in future work. The terrestrial specimens also differ from lunar minerals in their lower Fe content, absence of nanophase iron and space-weathering rims, and minor-element substitutions, which mainly rescale absolute property values and are not expected to reverse the relative inter-mineral ranking. Additionally, the properties used in the MCDM analysis were taken at fixed temperatures rather than at the processing temperatures above 1150 °C. C_p and κ were measured up to 200 °C, and tan δ was measured at room temperature. However, what enters the ranking is the relative ordering of the minerals, which is governed by crystal structure and bonding and does not invert upon heating. The thermal conductivity and diffusivity of silicate and oxide minerals decrease monotonically and similarly with temperature and preserve their order [70–72], and

the rank-stability analysis in Section 3.1 confirms this over the measured range. For tan δ, the room-temperature value is an appr[illegible] reas low-loss silicates do not [73–75]. This criterion is confirmed by our experiments at 1150 °C, where the densification sequence matched the prediction exactly with a Spearman's ρ of 1.000. The main residual concern is possible thermal runaway for minerals whose tan δ rises steeply at high temperature. This is a process-control issue rather than a reversal of the ranking, and high-temperature characterization remains a direction for future work. Second, five minerals with solidus temperatures exceeding 1650 °C could not be included in the TOPSIS ranking due to unmeasurable viscosity and surface tension; their potential roles as reinforcing phases in composite feedstocks remain unexplored. Third, although the subjectivity of fuzzy AHP has been mitigated through multi-expert fusion, entropy weighting, and Monte Carlo sensitivity analysis, future research could incorporate machine learning methods to further enhance the model's accuracy and generalizability. Finally, the gradient blending validation used controlled single-mineral perturbations of the CUG-1A matrix. Although this design verifies the directional effect of mineral enrichment or depletion, it does not fully capture nonlinear interactions in real multiphase lunar regolith, such as eutectic melting, solid-solution formation, interfacial reactions, and glass-assisted liquid formation. Future work should extend the validation to multicomponent regolith simulants with systematically varied mineral assemblages.

5. Conclusion

This study presents a systematic multi-criteria decision-making framework based on a thermophysical-property database of fifteen lunar-regolith-related minerals. The TOPSIS/VIKOR suitability ranking was performed for the ten minerals with complete decision matrices across three representative ISRU thermal manufacturing processes: HPS, MWS, and SLM. The principal conclusions are as follows:

(1) A comprehensive thermophysical database was established by measuring eight key parameters (solidus temperature, specific heat capacity, thermal conductivity, melt viscosity, surface tension, density, dielectric loss tangent, and solar absorptivity). The dataset reveals highly heterogeneous thermophysical profiles across the mineral set, with thermal conductivity varying by a factor of 3.1 and dielectric loss tangent by a factor of 9.9.

(2) Process-specific combined weights were determined through multiplicative normalization of Fuzzy-AHP and entropy weights. The dominant parameters are thermal conductivity (κ = 0.337) for HPS, dielectric loss tangent (tan δ = 0.573) for MWS, and solar absorptivity (α_{solar} = 0.330) for SLM, reflecting the distinct heat transfer mechanisms governing each process.

(3) TOPSIS and VIKOR dual ranking identified ilmenite as the only universally superior mineral, ranking first in all three processes (C_i=0.890, 0.976, and 0.780 for HPS, MWS, and SLM). The pyroxene group (enstatite, hedenbergite, augite) consistently ranked in the top tier for HPS and SLM, while the feldspar group (anorthite, albite, K-feldspar) ranked in the bottom tier across all processes. The two ranking methods showed high agreement (Spearman's ρ=0.830–0.976, $p < 0.01$).

(4) Sensitivity analyses confirmed the robustness of the rankings: Monte Carlo weight perturbation (±20%, 10,000 iterations) showed 28 of 30 mineral-process combinations with $\sigma < 1.0$, and VIKOR v-parameter variation (0.3–0.7) produced stable rankings for 9–10 of 10 minerals per process, with SLM achieving perfect stability.

(5) Gradient blending experiments validated the TOPSIS predictions at both macroscopic and microscopic scales. Cross-process density correlation yielded Pearson's r = 0.788 (p = 0.002) and Spearman's ρ = 0.825 (p = 0.001), with perfect within-process rank agreement (ρ = 1.000 for all three processes). Process-specific microstructural metrics (sintering degree for HPS and MWS, surface roughness for SLM) further corroborated the predicted rankings (Spearman's ρ = 1.000 where testable).

The findings provide first-order guidance for lunar ISRU applications: Ilmenite-enriched feedstocks obtained through magnetic beneficiation are suggested as promising raw materials for the three manufacturing processes, and the mineral suitability database established herein can serve as a preliminary screening tool for evaluating candidate landing sites based on their mineralogical composition.

Acknowledgments

This work was supported by the National Key Research and Development Program of China (2023YFB3711300), the Space Application System of China Manned Space Program (KJZ-YY-WCL404), and the Strategic Research and Consulting Project of the Chinese Academy of Engineering (2023-JB-09-10). Technical support from Huazhong University of Science & Technology Analysis & Testing Center was gratefully acknowledged.

References

[1] Zhou C, Gao Y, Zhou Y, She W, Shi Y, Ding L, et al. Properties and characteristics of regolith-based materials for extraterrestrial construction. Engineering 2024;37:159–81.
[2] Bao C, Zhang D, Wang Q, Cui Y, Feng P. Lunar in situ large-scale construction: quantitative evaluation of regolith solidification techniques. Engineering 2024;39:204–21.
[3] Han W, Zhang C, Sun J, Zhou C, Ding L. Experimental and numerical study on the structural behavior of assembled interlocking lunar landing pad. Acta Astronaut 2023;207:77–88.
[4] Hintze PE, Quintana S. Building a lunar or Martian launch pad with *in situ* materials: recent laboratory and field studies. J Aerosp Eng 2013;26(1):134–42.
[5] Taylor LA, Meek TT. Microwave sintering of lunar soil: properties, theory, and practice. J Aerosp Eng 2005;18(3):188–96.
[6] Farries KW, Visintin P, Smith ST, van Eyk P. Sintered or melted regolith for lunar construction: state-of-the-art review and future research directions. Constr Build Mater 2021;296:123627.

Journal Pre-proofs

[7] Han W, Li X, Cai L, Xia Y, Zhou Y, Zhou C, et al. Vacuum sintering of HUST-1 lunar regolith simulants with different particle sizes. Constr Build Mate
[8] Ding M, Chen X, Li Y, Song L, Shi Y, Luo L, et al. Vacuum sintering of the self-developed Chang'E-5 lunar regolith simulant. Constr Build Mater 2024;438:137343.
[9] Wan F, Zuo Y, Pan Y, Yu A, Qi J, Lu X. Iron-enhanced simulated lunar regolith sintered blocks: preparation, sintering and mechanical properties. Constr Build Mater 2024;439:137395.
[10] Gholami S, Zhang X, Kim YJ, Kim YR, Cui B, Shin HS, et al. Hybrid microwave sintering of a lunar soil simulant: effects of processing parameters on microstructure characteristics and mechanical properties. Mater Des 2022;220:110878.
[11] Wang Z, Zheng Z, Jiang L, Qin Y, Zhu J, Zhou Y, et al. Microwave sintering of HUST-2 lunar highland regolith simulant: effects on microstructure evolution, mechanical and thermal properties. Constr Build Mater 2025;467:140391.
[12] Liu Z, Li J, Liu C, Guo J, Guo Z, Yuan S, et al. Vacuum susceptor-assisted microwave sintering of lunar regolith simulant bricks: a potential pathway for extraterrestrial construction. Constr Build Mater 2026;523:146289.
[13] Lu JQ, Li ZW, Feng XT, He CD, Wang YJ, Zuo Y, et al. Microwave melting of lunar regolith simulant in an unchambered environment: insights from physical model experiments. Int J Rock Mech Min Sci 2026;200:106433.
[14] Dang F, Zhu J, Ke M, Wang Z, Wen S, Zhou Y, et al. Effects of different laser scanning strategies on the morphology, microstructure, and mechanical properties of lunar regolith simulant formed by laser powder bed fusion. Addit Manuf Front 2025;5(1):200283.
[15] Sun W, Dang F, Zhou Y, Wen S, Zhou C, Shi Y, et al. Additive manufacturing of lunar regolith: a review. Addit Manuf Front 2025;4(3):200225.
[16] Yang H, Wang H, Xie B, Sun M, Chen S, Zhang Z, et al. Feasibility study and prospects analysis of lunar regolith forming based on concentrated solar energy. Acta Astronaut 2025;232:424–38.
[17] Wang R, Qiao G. Direct concentrating solar powder bed fusion for lunar in-situ manufacturing: processing methodology and performance enhancement. J Manuf Process 2025;154:546–62.
[18] Zhang X, Liu Y, Zhao S, Song J, Yao W, Wang W, et al. Melting and rapid solidification of lunar regolith particles returned by Chang'E-5 Mission. Research 2024;7:0486.
[19] Meurisse A, Beltzung J, Kolbe M, Cowley A, Sperl M. Influence of mineral composition on sintering lunar regolith. J Aerosp Eng 2017;30(4):04017014.
[20] Guardabasso P, Paternostro S, Bedialauneta P, Fonteyne R. Lunar landing necessary building blocks and good practices for a sustainable development of human lunar activities. Acta Astronaut 2023;202:782–90.
[21] Yang C, Zhang X, Bruzzone L, Liu B, Liu D, Ren X, et al. Comprehensive mapping of lunar surface chemistry by adding Chang'E-5 samples with deep learning. Nat Commun 2023;14(1):7554.
[22] Li P, Yu J, Zhu W, Li Y, Gao P, Han Y, et al. An innovative process for recovery of ilmenite using mineral phase transformation followed by magnetic separation. Adv Powder Technol 2024;35(7):104540.
[23] Kawamoto H, Morooka H, Nozaki H. Improved electrodynamic particle-size sorting system for lunar regolith. J Aerosp Eng 2022;35(1):04021115.
[24] Mitchell K, Urade S, Kershaw A, Chu P, Jin Y. 3D printing of conical centrifuge system for mineral particle separation. Separ Purif Tech 2023;306:122567.
[25] Rasera J, Cilliers J, Lamamy J, Hadler K. The beneficiation of lunar regolith for space resource utilisation: a review. Planet Space Sci 2020;186:104879.
[26] Isachenkov M, Grande AM, Mariani M, Lecis N, Casati R, Silvestroni L, et al. Magnetic beneficiation–a novel approach to facilitate additive manufacturing of lunar regolith ceramics by vat photopolymerization. Addit Manuf 2025;109:104863.
[27] Isachenkov M, Grande AM, Sala G. Optimizing lunar regolith for vat polymerization and sintering: pre-processing & mineral composition impact. Ceram Int 2024;50(18):32265–77.
[28] Kulkarni K, Fabien Frank M, Jundullah Hanafi MI, Gesing TM, Zabel P. Optimizing lunar regolith beneficiation for ilmenite enrichment. Front Space Technol 2024;4:1328341.
[29] Reiss P, Grill L, Barber S. Thermal extraction of volatiles from the lunar regolith simulant NU-LHT-2M: preparations for in-situ analyses on the Moon. Planet Space Sci 2019;175:41–51.
[30] Li Y, Liu J, Yue Z. NAO-1: lunar highland soil simulant developed in China. J Aerosp Eng 2009;22(1):53–57.
[31] Li C, Hu H, Yang MF, Pei ZY, Zhou Q, Ren X, et al. Characteristics of the lunar samples returned by the Chang'E-5 mission. Natl Sci Rev 2021;9(2):nwab188.
[32] Li C, Hu H, Yang MF, Liu J, Zhou Q, Ren X, et al. Nature of the lunar far-side samples returned by the Chang'E-6 mission. Natl Sci Rev 2024;11(11):nwae328.
[33] Su B, Zhang D, Chen Y, Yang W, Mao Q, Li XH, et al. Low Ni and Co olivine in Chang'E-5 basalts reveals the origin of the young volcanism on the Moon. Sci Bull 2023;68(17):1918–27.
[34] Tian HC, Wang H, Chen Y, Yang W, Zhou Q, Zhang C, et al. Non-KREEP origin for Chang'E-5 basalts in the Procellarum KREEP Terrane. Nature 2021;600(7887):59–63.
[35] He Q, Cao Z, Qian Y, Hui H, Baziotis I, Xiao L, et al. Petrogenesis of magnesian troctolitic clasts from Chang'E-5 drilling sample: implications for the origin of ejecta material from lunar highlands. Icarus 2024;408:115853.
[36] Zeng X, Li X, Liu J. Exotic clasts in Chang'E-5 regolith indicative of unexplored terrane on the Moon. Nat Astron 2023;7(2):152–59.
[37] Li QL, Zhou Q, Liu Y, Xiao Z, Lin Y, Li JH, et al. Two-billion-year-old volcanism on the Moon from Chang'E-5 basalts. Nature 2021;600(7887):54–8.
[38] Yang J, Du W. High-pressure minerals and new lunar mineral Changesite-(Y) in Chang'E-5 regolith. Matter Radiat Extrem 2024;9(2):027401.
[39] Li JH, Li QL, Zhao L, Zhang JH, Tang X, Gu LX, et al. Rapid screening of Zr-containing particles from Chang'E-5 lunar soil samples for isotope geochronology: Technical roadmap for future study. Geosci Front 2022;13(3):101367.
[40] Liu X, Gu L, Tian HC, Li J, Tang X, Hu S, et al. First classification of iron meteorite fragment preserved in Chang'E-5 lunar soils. Sci Bull 2024;69(4):554–61.
[41] Pang R, Yang J, Du W, Zhang A, Liu S, Li R. New occurrence of seifertite and stishovite in Chang'E-5 regolith. Geophys Res Lett 2022;49(12):e2022GL098722.
[42] Deer WA, Howie RA, Zussman J. An introduction to the rock-forming minerals. London: Mineralogical Society of Great Britain and Ireland; 2013.
[43] Gueymard CA. The sun's total and spectral irradiance for solar energy applications and solar radiation models. Sol Energy 2004;76(4):423–53.
[44] Buckley JJ. Fuzzy hierarchical analysis. Fuzzy Sets Syst 1985;17(3):233–47.
[45] Buckley JJ. Ranking alternatives using fuzzy numbers. Fuzzy Sets Syst 1985;15(1):21–31.
[46] Chang DY. Applications of the extent analysis method on fuzzy AHP. Eur J Oper Res 1996;95:649–55.
[47] Shannon CE. A mathematical theory of communication. Bell Syst Tech J 1948;27(3):379–423.
[48] Zou ZH, Yun Y, Sun JN. Entropy method for determination of weight of evaluating indicators in fuzzy synthetic evaluation for water quality assessment. J Environ Sci 2006;18(5):1020–23.
[49] Wang YM, Luo Y. Integration of correlations with standard deviations for determining attribute weights in multiple attribute decision making. Math Comput Model 2010;51(1–2):1–12.
[50] Hwang CL, Yoon K. Multiple attribute decision making: methods and applications a state-of-the-art survey. New York City: Springer Science & Business Media; 2012.

Journal Pre-proofs

[51] Opricovic S, Tzeng GH. Compromise solution by MCDM methods: a comparative analysis of VIKOR and TOPSIS. Eur J Oper Res 2004;156:445–55.
Journal Pre-proofs
[52] Opricovic S, Tzeng GH. Extended VIKOR method in comparison with outranking methods. Eur J Oper Res 2007;178:514–29.
[53] Fukuyama H, Donald J, Toguri J. Wetting behavior and interfacial reaction between fayalite slag and MgO. In: Proceedings of the 125th TMS Annual Meeting; 1996 Feb 5–8; Anaheim, CA, USA. New York City: The Minerals, Metals and. Materials Society (TMS); 1996.
[54] Taniguchi H. Surface tension of melts in the system $CaMgSi_2O_6$-$CaAl_2Si_2O_8$ and its structural significance. Contrib Mineral Petrol 1988;100(4):484–9.
[55] Walker D, Mullins Jr O. Surface tension of natural silicate melts from 1,200–1,500 C and implications for melt structure. Contrib Mineral Petrol 1981;76(4):455–62.
[56] Bottinga Y, Weill DF. The viscosity of magmatic silicate liquids: a model for calculation. Report. Paris: Louis Barrabé Geochemical Research Group; 1971.
[57] Shartsis L, Spinner S. Surface tension of molten alkali silicates. J Res Natl Bur Stand 1951;46(5):385–90.
[58] Mills K, Keene B. Physical properties of BOS slags. Int Mater Rev 1987;32(1):1–120.
[59] Taniguchi H, Murase T. Some physical properties and melt structures in the system diopside-anorthite. J Volcanol Geotherm Res 1987;34(1–2):51–64.
[60] Chen T, Dutrizac J, Haque K, Wyslouzil W, Kashyap S. The relative transparency of minerals to microwave radiation. Can Metall Q 1984;23(3):349–51.
[61] Guo Z, Li C, Li Y, Wen Y, Tai K, Li X, et al. Nanophase iron particles derived from fayalitic olivine decomposition in Chang'E-5 lunar soil: Implications for thermal effects during impacts. Geophys Res Lett 2022;49(5):e2021GL097323.
[62] Pieters CM, Taylor LA, Noble SK, Keller LP, Hapke B, Morris RV, et al. Space weathering on airless bodies: resolving a mystery with lunar samples. Meteorit Planet Sci 2000;35(5):1101–7.
[63] Hapke B. Space weathering from Mercury to the asteroid belt. J Geophys Res 2001;106(E5):10039–73.
[64] Zhao R, Shen L, Xiao D, Chang C, Huang Y, Yu J, et al. Diverse glasses revealed from Chang'E-5 lunar regolith. Natl Sci Rev 2023;10(12):nwad079.
[65] Kuczynski GC. Self-diffusion in sintering of metallic particles. Berlin: Springer; 1990. p. 509–27.
[66] Taran MN. Electronic intervalence Fe^{2+}+ Ti^{4+}→ Fe^{3+}+ Ti^{3+} charge-transfer transition in ilmenite. Phys Chem Miner 2019;46(9):839–43.
[67] Mattson SM, Rossman GR. Fe^{2+}-Ti^{4+} charge transfer in stoichiometric Fe^{2+}, Ti^{4+}-minerals. Phys Chem Miner 1988;16(1):78–82.
[68] Chiteme C, Mulaba-Bafubiandi A. An investigation on electrical properties of microwave treated natural ilmenite ($FeTiO_3$). J Mater Sci 2006;41(8):2365–72.
[69] Seda T, Hearne G. Pressure induced Fe^{2+}+ Ti^{4+}→ Fe^{3+}+ Ti^{3+} intervalence charge transfer and the Fe^{3+}/Fe^{2+} ratio in natural ilmenite ($FeTiO_3$) minerals. J Phys Condens Matter 2004;16(15):2707–18.
[70] Hofmeister AM. Mantle values of thermal conductivity and the geotherm from phonon lifetimes. Science 1999;283(5408):1699–706.
[71] Pertermann M, Hofmeister AM. Thermal diffusivity of olivine-group minerals at high temperature. Am Mineral 2006;91(11–12):1747–60.
[72] Höfer M, R F. Heat transfer in quartz, orthoclase, and sanidine at elevated temperature. Phys Chem Miner 2002;29(9):571–84.
[73] Kitchen HJ, Vallance SR, Kennedy JL, Tapia-Ruiz N, Carassiti L, Harrison A, et al. Modern microwave methods in solid-state inorganic materials chemistry: from fundamentals to manufacturing. Chem Rev 2014;114(2):1170–206.
[74] Guo X, Feng B, Zhang B, Zhai S, Xue W, Song Y, et al. Effect of iron content on the thermal conductivity and thermal diffusivity of orthopyroxene. Geochem Geophys Geosyst 2024;25(6):e2023GC011419.
[75] Branlund JM, Hofmeister AM. Heat transfer in plagioclase feldspars. Am Mineral 2012;97(7):1145–54.

Thermophysical database of 15 lunar minerals with 120 self-measured data points

Fuzzy-AHP + entropy + TOPSIS/VIKOR framework for mineral suitability ranking

Complete mineral suitability ranking established for three ISRU processes

Process-dominant parameters: κ for HPS, tan δ for MWS, α_{solar} for SLM

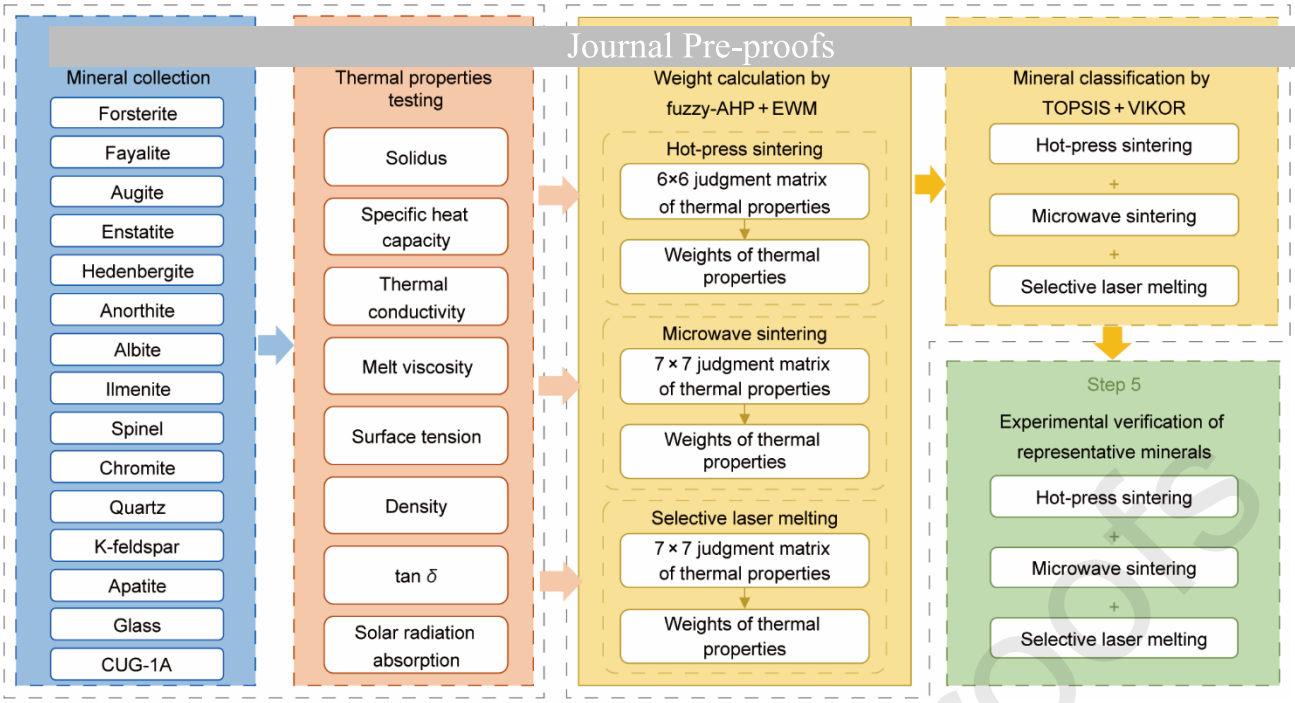
Gradient blending experiments validate predictions with Spearman ρ=1.000

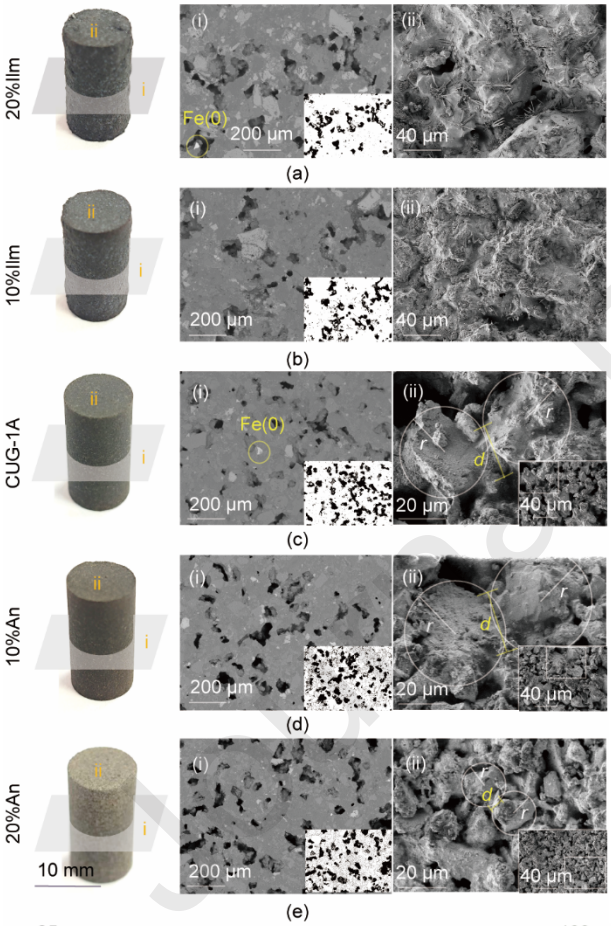
Declaration of Competing Interest

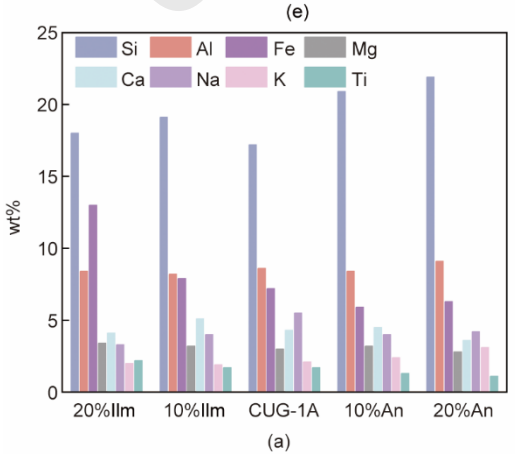
The authors declare that they have no known competing financial interests or personal relationships that could have appeared to influence the work reported in this paper.

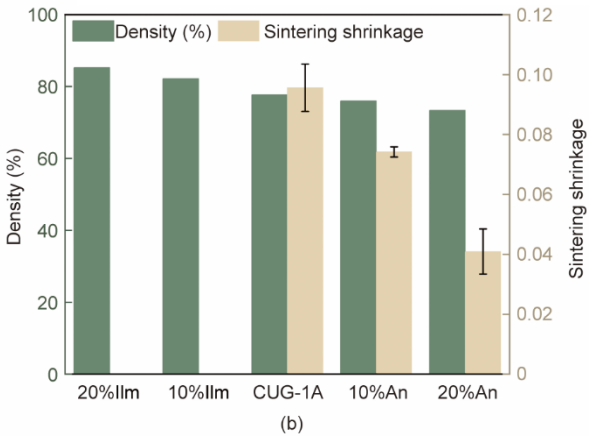
Journal Pre-proofs

Journal Pre-proofs

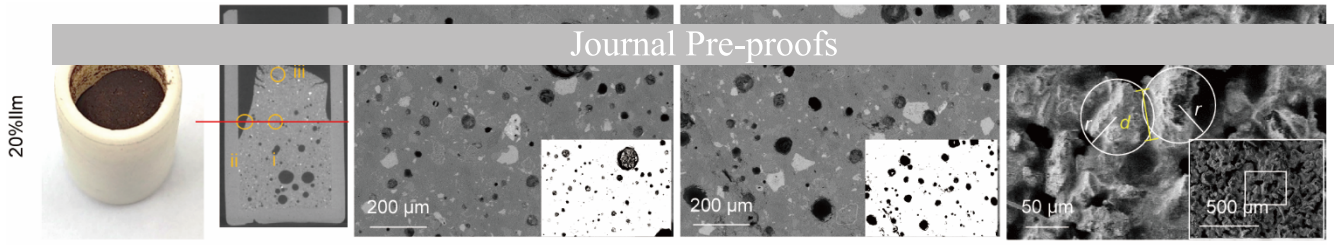




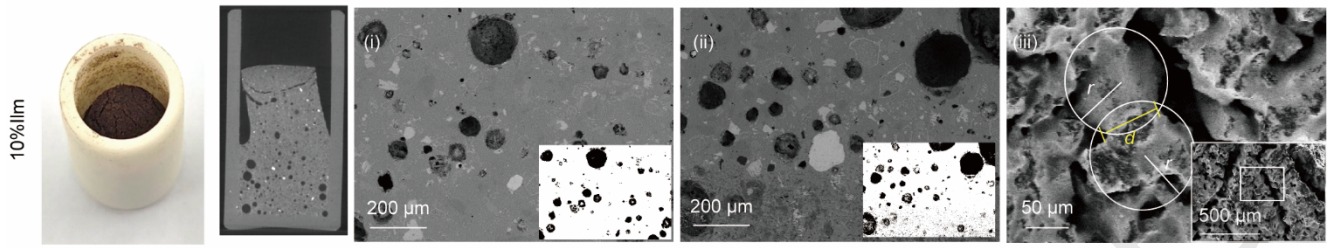




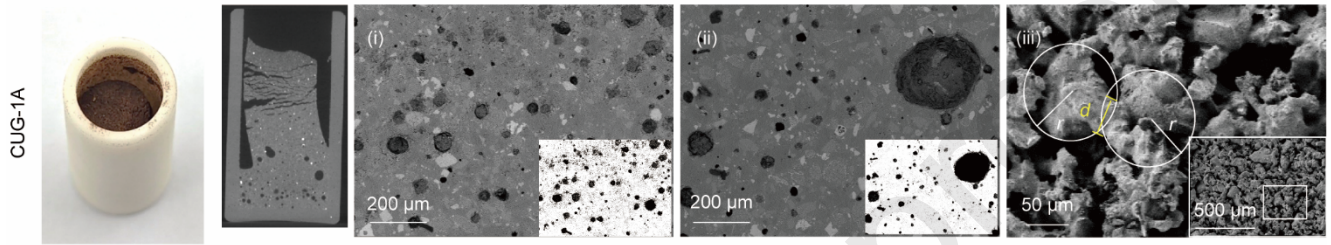
Journal Pre-proofs



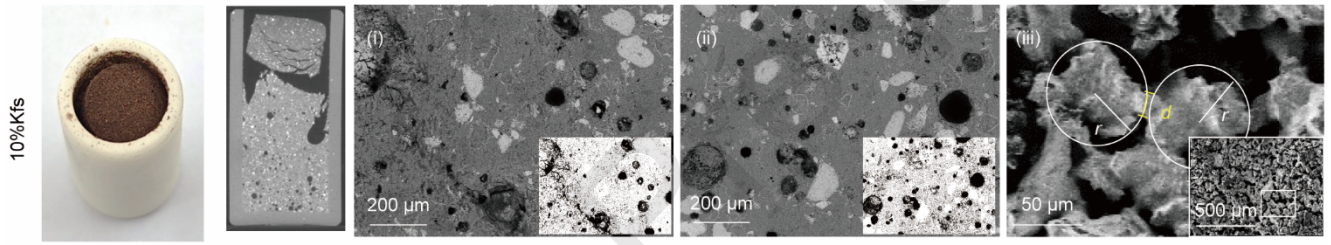
(a)



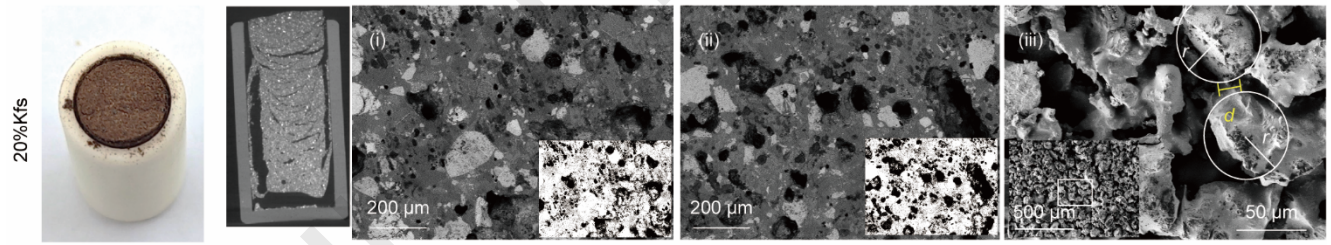
(b)



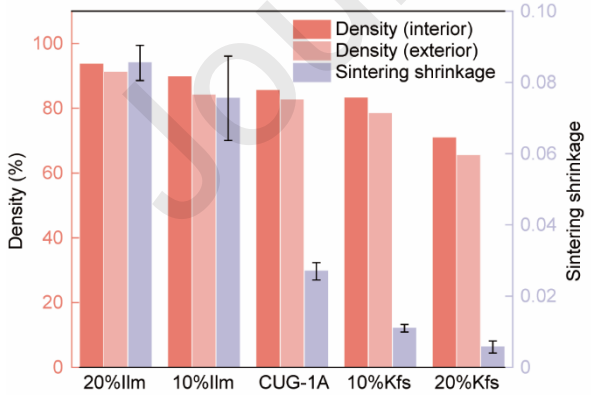
(c)

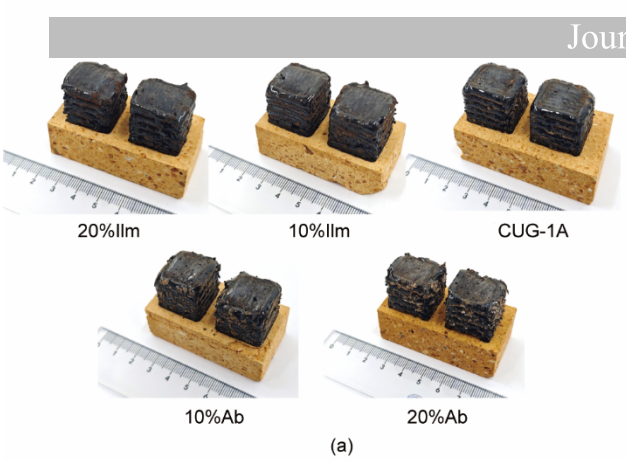


(d)

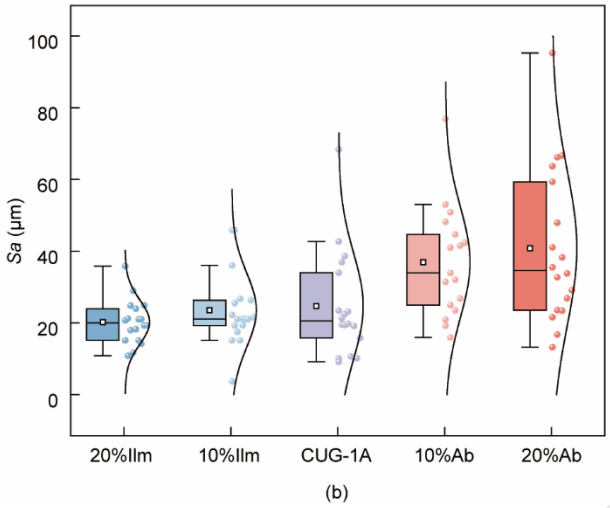


(e)

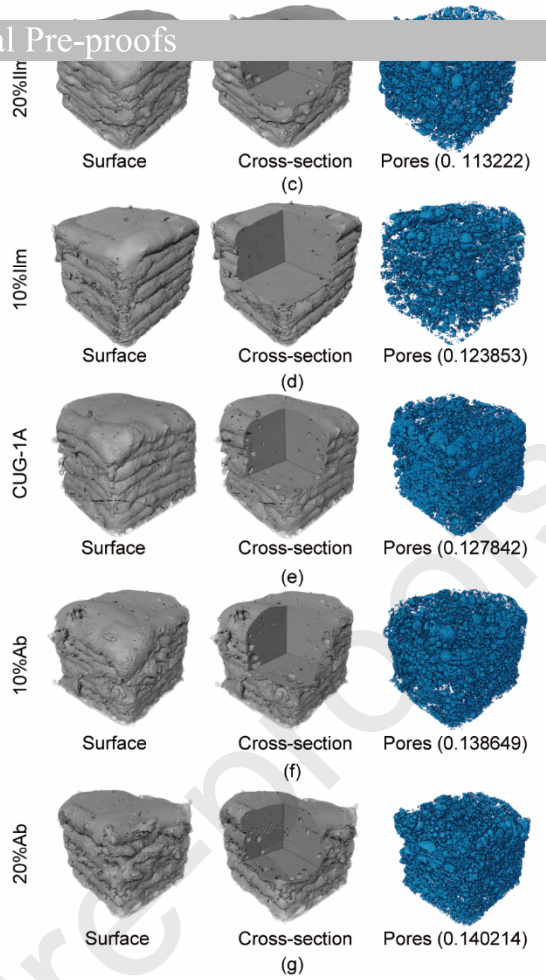




(a)

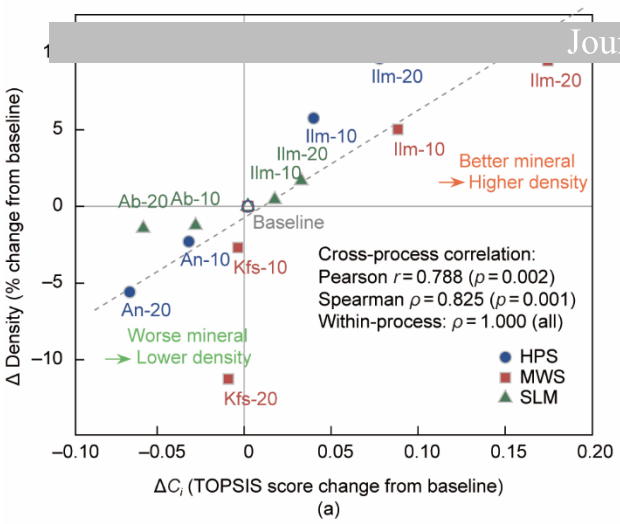


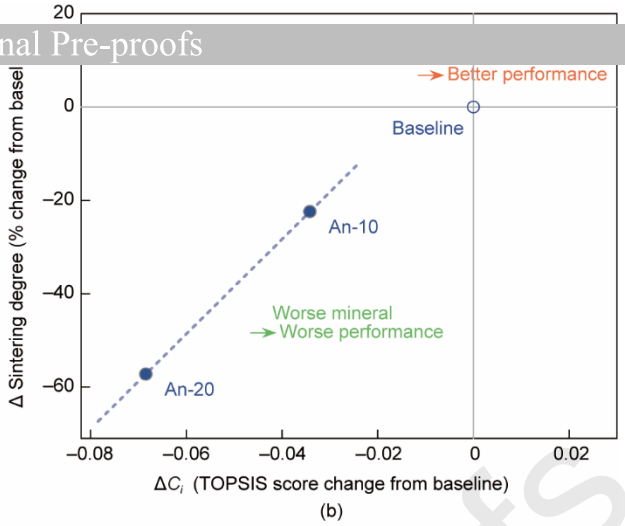
(b)

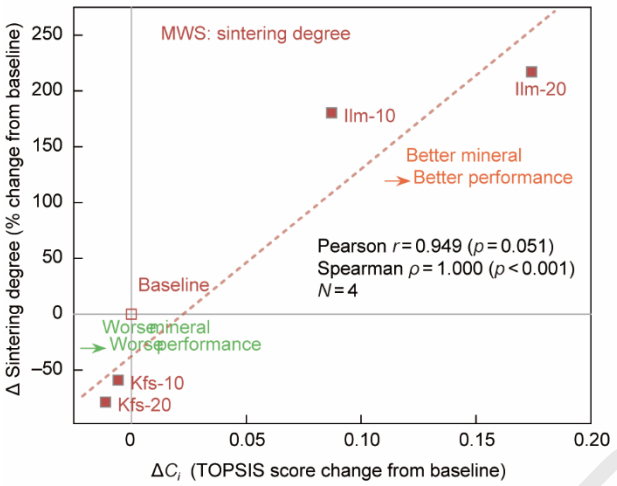


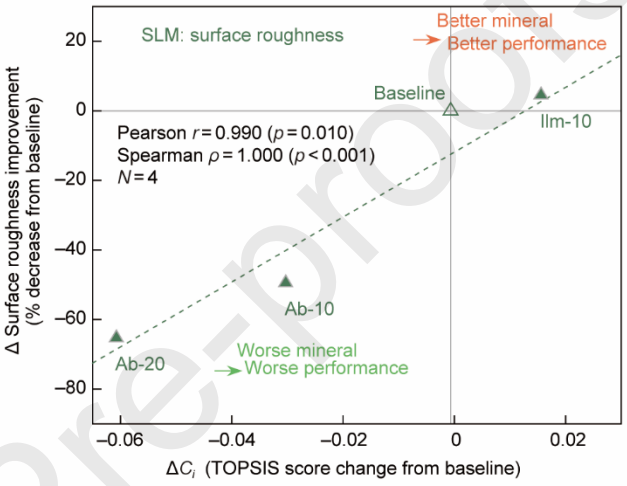
Journal Pre-proofs

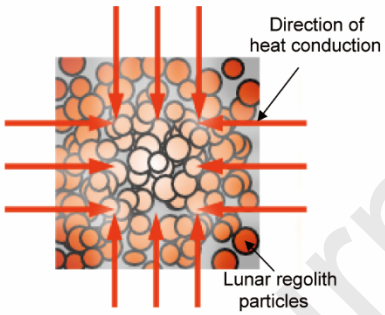
Journal Pre-proofs

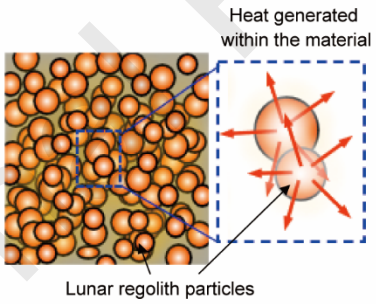


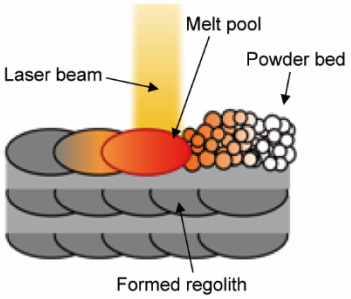




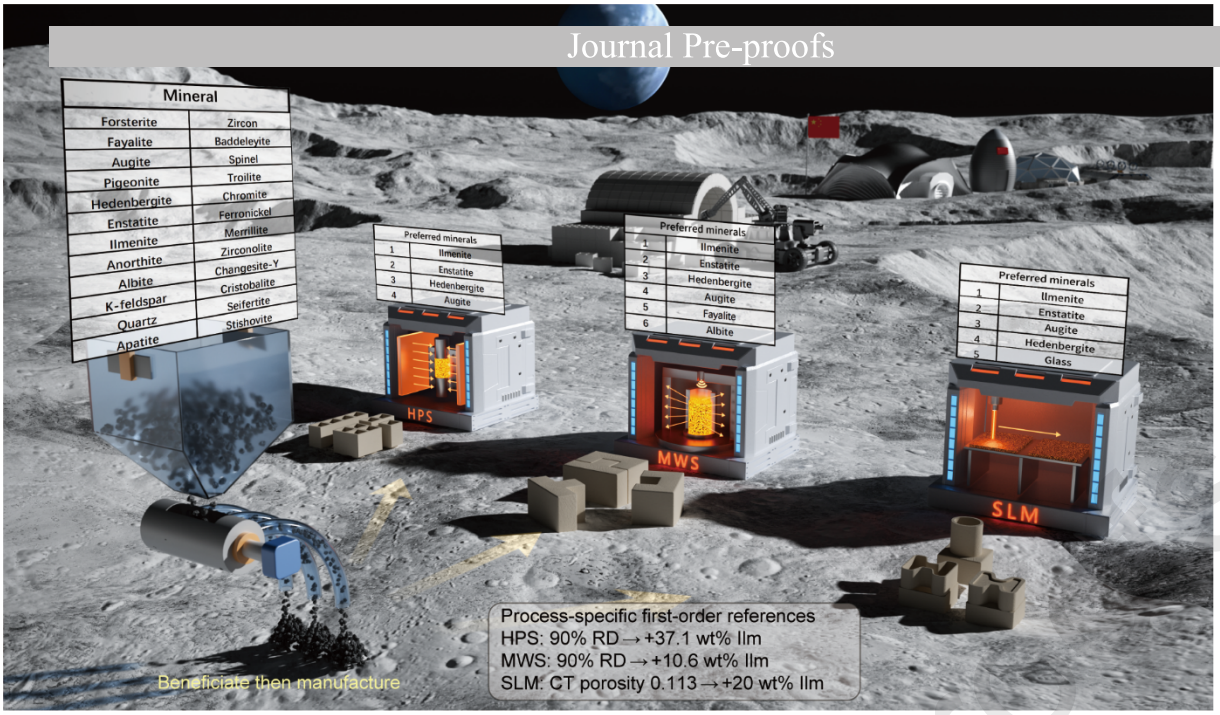








Journal Pre-proofs




Forsterite


Fayalite


Augite


Enstatite


Hedenbergite


Ilmenite


Anorthite


Albite


K-feldspar


Quartz


Apatite

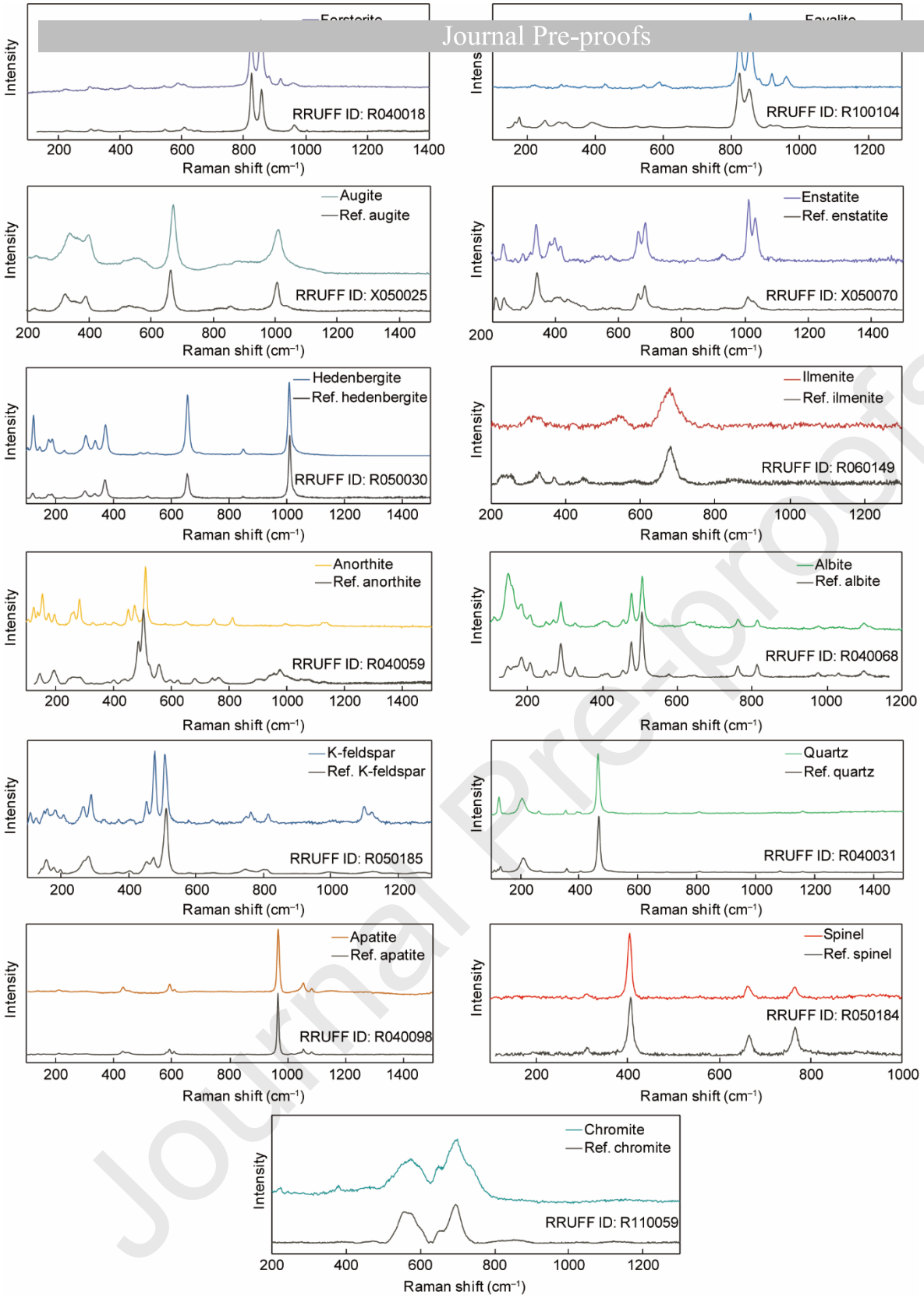

Spinel


Chromite


Glass

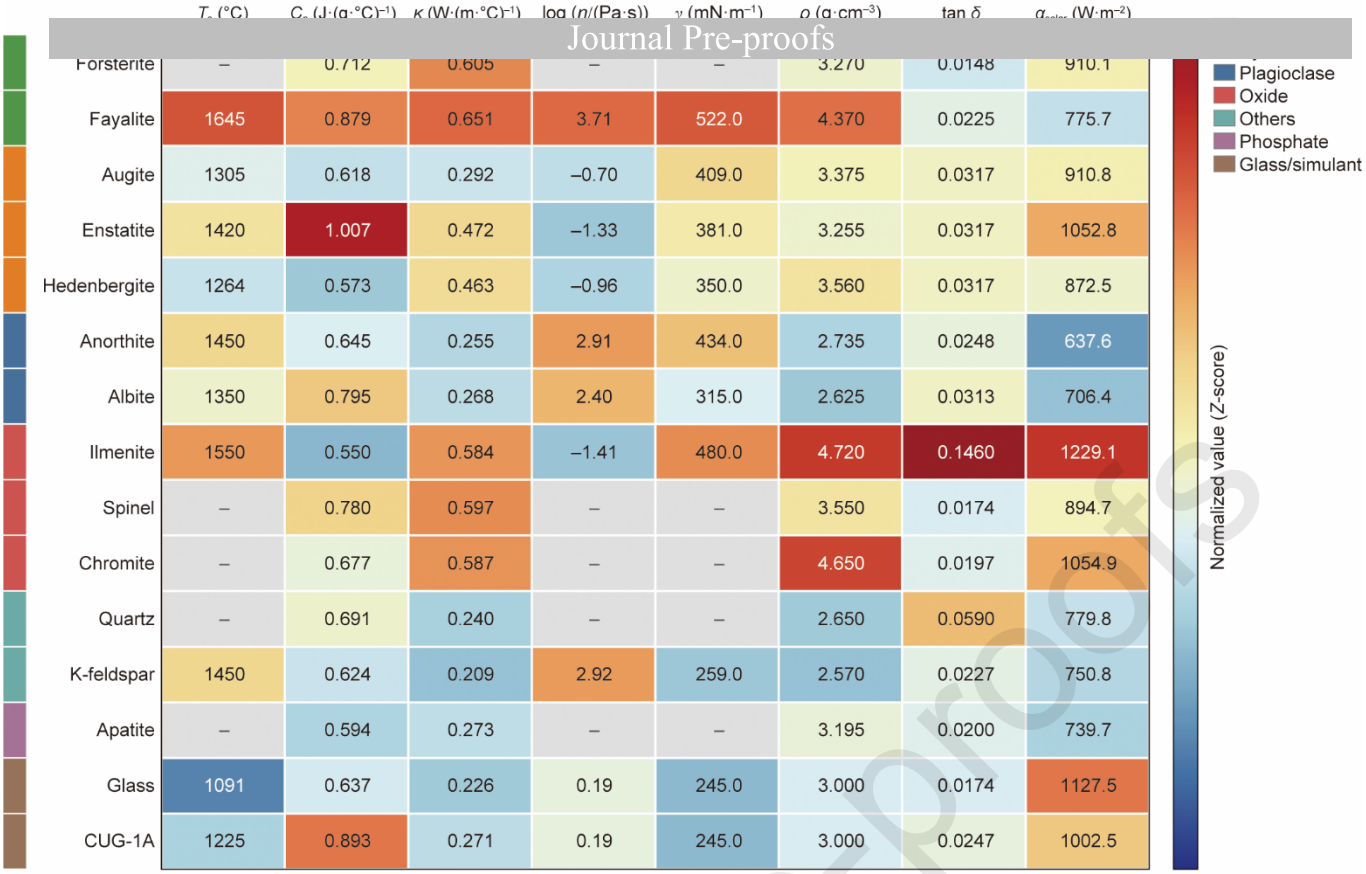
Journal Pre-proofs

Journal Pre-proofs



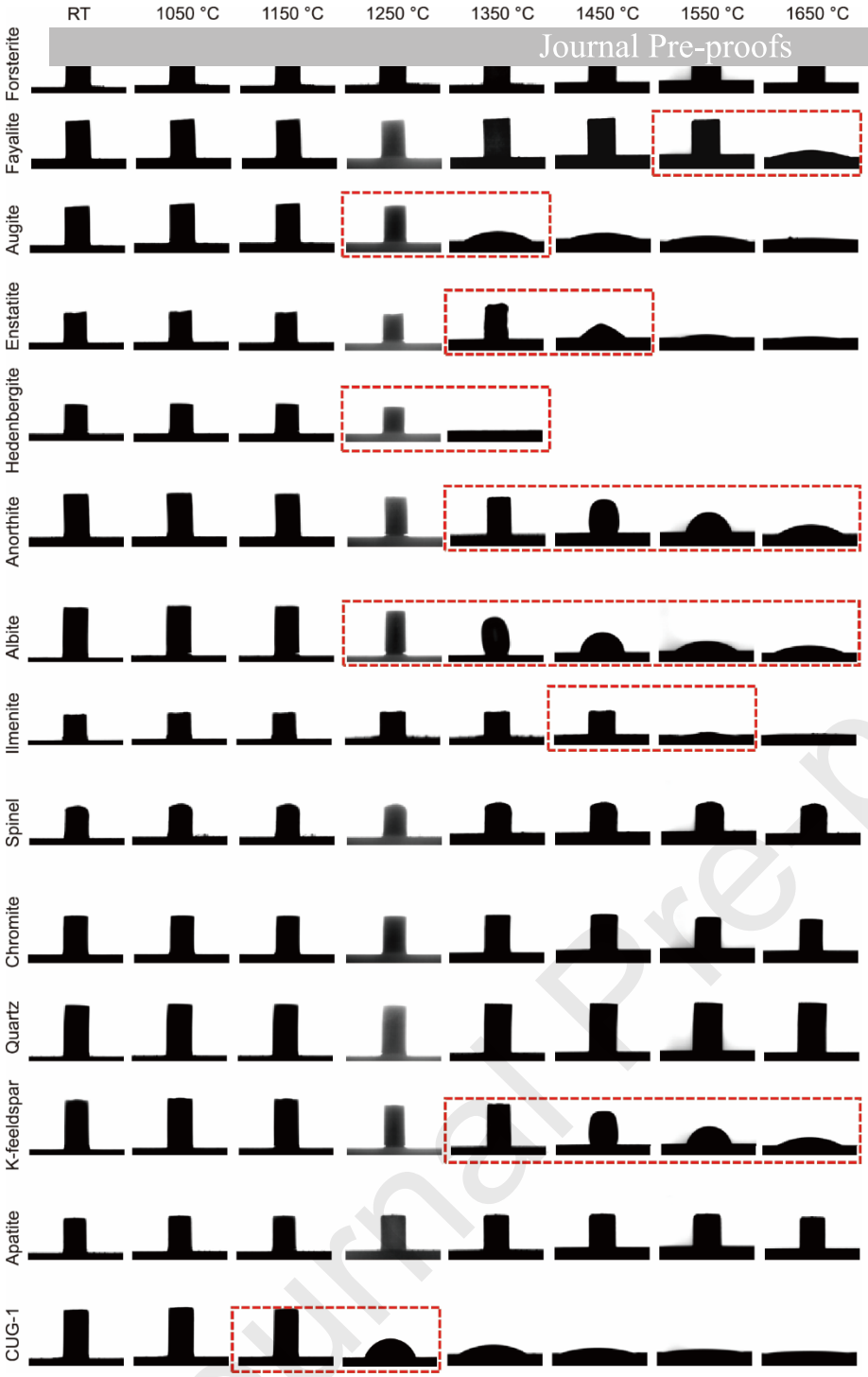
Journal Pre-proofs

Journal Pre-proofs



Journal Pre-proofs

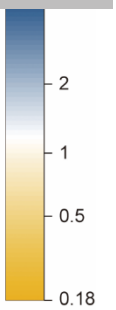
Journal Pre-proofs



Journal Pre-proofs

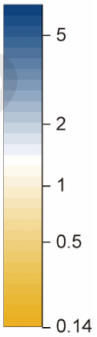
Journal Pre-proofs

	T_s	C_p	κ	η	γ	ρ
T_s						
C_p	(0.177, 0.215, 0.275)	(1, 1, 1)	(0.218, 0.281, 0.397)	(0.437, 0.585, 0.794)	(1.101, 1.357, 1.817)	(0.874, 1.145, 1.587)
κ	(0.481, 0.630, 1.000)	(2.520, 3.557, 4.579)	(1, 1, 1)	(1, 1.494, 2.080)	(2.289, 3.476, 4.579)	(2.520, 3.557, 4.579)
η	(0.397, 0.606, 0.909)	(1.260, 1.710, 2.289)	(0.481, 0.669, 1.000)	(1, 1, 1)	(2.000, 3.107, 4.160)	(2.000, 2.466, 4.160)
γ	(0.177, 0.210, 0.275)	(0.550, 0.737, 0.909)	(0.218, 0.288, 0.437)	(0.240, 0.322, 0.500)	(1, 1, 1)	(0.550, 0.737, 0.909)
ρ	(0.161, 0.193, 0.240)	(0.630, 0.874, 1.145)	(0.218, 0.281, 0.397)	(0.240, 0.405, 0.500)	(1.101, 1.357, 1.817)	(1, 1, 1)



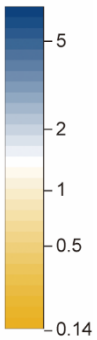
(a)

	T_s	C_p	κ	η	γ	ρ	tan δ
T_s	(1, 1, 1,)	(3.175, 4.217, 5.241)	(0.693, 1.000, 1.442)	(1.260, 2.289, 3.302)	(3.634, 4.762, 5.646)	(3.302, 4.380, 5.429)	(0.303, 0.437, 0.794)
C_p	(0.191, 0.237, 0.315)	(1, 1, 1)	(0.232, 0.303, 0.437)	(0.550, 0.794, 1.260)	(1.587, 1.710, 1.817)	(0.874, 1.442, 2.289)	(0.138, 0.160, 0.191)
κ	(0.693, 1.000, 1.442)	(2.289, 3.302, 4.309)	(1, 1, 1)	(2.000, 2.466, 2.884)	(3.302, 4.380, 5.429)	(2.520, 3.684, 4.762)	(0.405, 0.500, 0.693)
η	(0.303, 0.437, 0.794)	(0.794, 1.260, 1.817)	(0.347, 0.405, 0.500)	(1, 1, 1)	(2.000, 3.107, 4.160)	(1.587, 2.621, 3.634)	(0.188, 0.232, 0.303)
γ	(0.177, 0.210, 0.275)	(0.550, 0.585, 0.630)	(0.184, 0.228, 0.303)	(0.240, 0.322, 0.500)	(1, 1, 1)	(0.382, 0.585, 0.909)	(0.144, 0.168, 0.203)
ρ	(0.184, 0.228, 0.303)	(0.437, 0.693, 1.145)	(0.210, 0.271, 0.397)	(0.275, 0.382, 0.630)	(1.101, 1.710, 2.621)	(1, 1, 1)	(0.138, 0.155, 0.184)
tan δ	(1.260, 2.289, 3.302)	(5.241, 6.257, 7.268)	(1.442, 2.000, 2.466)	(3.302, 4.309, 5.313)	(4.932, 5.944, 6.952)	(5.429, 6.463, 7.230)	(1, 1, 1)



(b)

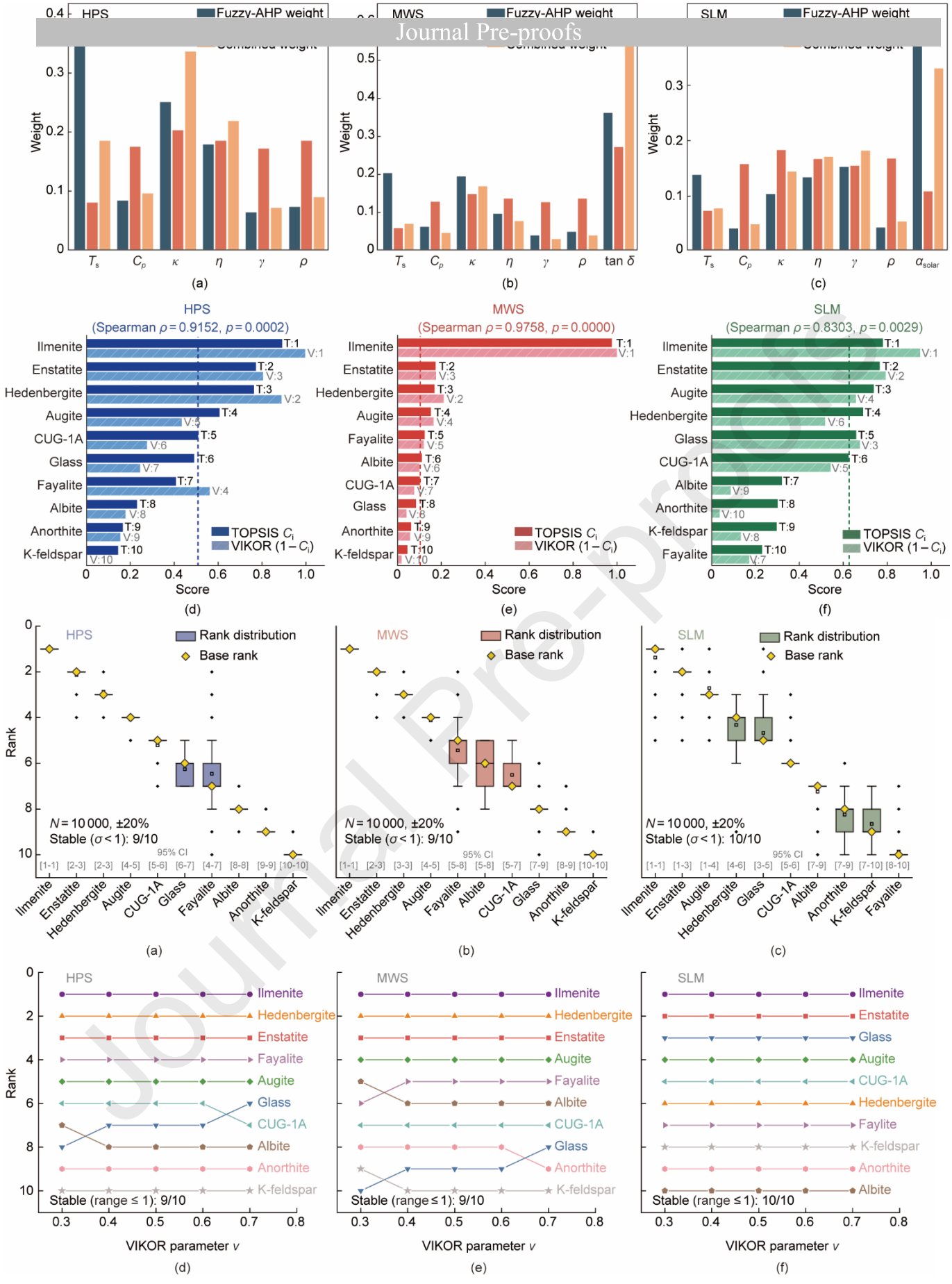
	T_s	C_p	κ	η	γ	ρ	α_{solar}
T_s	(1, 1, 1,)	(3.634, 4.718, 5.769)	(1.000, 1.442, 2.000)	(0.693, 1.000, 1.442)	(0.481, 0.794, 1.442)	(2.520, 3.780, 4.762)	(0.203, 0.255, 0.347)
C_p	(0.173, 0.212, 0.275)	(1, 1, 1)	(0.240, 0.322, 0.500)	(0.200, 0.250, 0.333)	(0.193, 0.240, 0.322)	(0.874, 1.145, 1.587)	(0.131, 0.150, 0.177)
κ	(0.500, 0.693, 1.000)	(2.000, 3.107, 4.160)	(1, 1, 1)	(0.437, 0.693, 1.145)	(0.382, 0.585, 0.909)	(2.289, 2.714, 4.481)	(0.223, 0.292, 0.437)
η	(0.693, 1.000, 1.442)	(3.000, 4.000, 5.000)	(0.874, 1.442, 2.289)	(1, 1, 1)	(0.693, 0.794, 1.000)	(2.289, 3.476, 4.579)	(0.207, 0.265, 0.368)
γ	(0.693, 1.260, 2.080)	(3.107, 4.160, 5.192)	(1.101, 1.710, 2.621)	(1.000, 1.260, 1.442)	(1, 1, 1)	(2.289, 3.476, 4.579)	(0.218, 0.281, 0.397)
ρ	(0.210, 0.265, 0.397)	(0.630, 0.874, 1.145)	(0.223, 0.368, 0.437)	(0.218, 0.288, 0.437)	(0.218, 0.288, 0.437)	(1, 1, 1)	(0.138, 0.155, 0.184)
α_{solar}	(2.884, 3.915, 4.932)	(5.646, 6.649, 7.652)	(2.289, 3.420, 4.481)	(2.714, 3.780, 4.820)	(2.520, 3.557, 4.579)	(5.429, 6.463, 7.230)	(1, 1, 1)



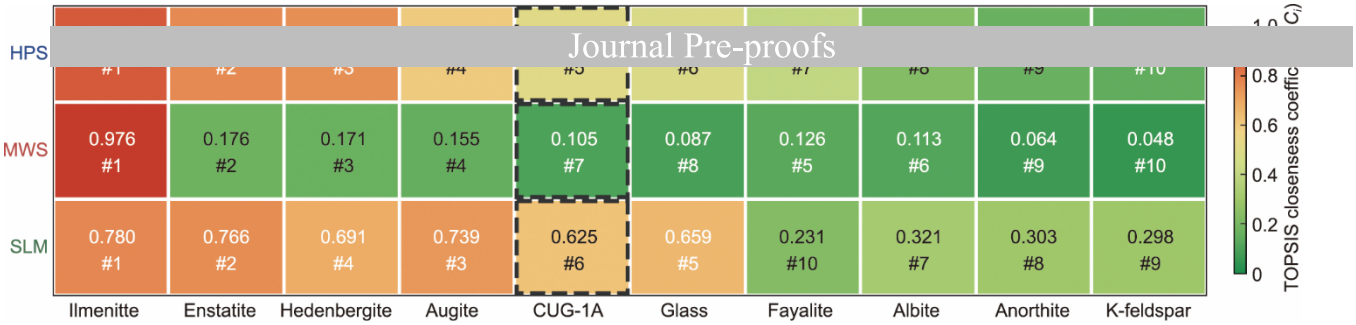
(c)

Journal Pre-proofs

Journal Pre-proofs



Journal Pre-proofs



Journal Pre-proofs